Bioelectric signaling and the control of cardiac cell identity in response to mechanical forces

Hajime Fukui, Renee Wei-Yan Chow, Jing Xie, Yoke Yin Foo, Choon Hwai Yap, Nicolas Minc, Naoki Mochizuki, Julien Vermot

Molecular control of endocardial cell fate in response to mechanical forces during cardiac valve formation

Hajime Fukui[1,2], Renee Wei-Yan Chow[1], Jing Xie[3], Vivek Vasudevan[4], Choon Hwai Yap[4,5], Nicolas Minc[3], Naoki Mochizuki[2] and Julien Vermot[1,5]

[1] Institut de Génétique et de Biologie Moléculaire et Cellulaire (IGBMC), Centre National de la Recherche Scientifique UMR7104, Institut National de la Santé et de la Recherche Médicale U1258 and Université de Strasbourg, Illkirch, France

[2] Department of Cell Biology, National Cerebral and Cardiovascular Center Research Institute, Suita, Japan

[3] Université de Paris, Centre National de la Recherche Scientifique UMR7592, Institut Jacques Monod, Paris, France

[4] Department of Biomedical Engineering, National University of Singapore, Singapore, Singapore

[5] Department of Bioengineering, Imperial College London, London, United Kingdom

Abstract

Developing cardiovascular systems use mechanical forces at all organizational scales to shape tissue. How ubiquitous blood flow forces instruct local cardiac cell identity is still unclear. By manipulating mechanical forces *in vivo*, we show that ectopic shear stress is necessary and sufficient to promote ectopic valve like structure by activating cellular valve identity and Endothelial to Mesenchymal Transition. We found ectopic valve formation results from the activation of two mechanosensitive pathways acting in parallel, the well-established TRP-klf2a-wnt9b axis and an extracellular ATP-dependent purinergic receptor pathway specifically triggering Ca2+ oscillation and Nfatc1 activation. Thus, mechanical forces are converted into discrete bioelectric signals by synergistic mechanosensitive pathways to generate positional information and control valve formation.

Main Text:

The cardiovascular system is continuously exposed to mechanical forces, such as fluid shear stresses and stretching forces generated by blood flow and heartbeat. The mechanotransduction cascade translates forces into cellular biochemical signals in the cell (*1, 2*). The lumen of the cardiovascular system is lined by endocardial cells (EdCs) and endothelial cells (ECs). These cell types present unique functional properties and differentially respond to forces depending on the type of blood vessels or heart regions they belong to (*3-6*). Heart valve defects are common human congenital anomalies, with an incidence close to 2% of live births (*7*). While a number of valvular heart defects have been linked to specific genetic mutations (e.g., in *NOTCH1*, *TBX5*, *GATA4*, *TBX20*, *LMCD1*, *TNS1*, and *DCHS1*) (*8-12*), the majority have no clear environmental or genetical cause (*13*). Thus, it is thought that non genetically encoded factors play an essential role in the genesis of congenital valve defects. The forces generated in the heart are significantly higher than in the vascular system where pathologies related to mechanical forces start to be well established (*14*, *15*). Consequently, the molecular mechanisms underlying force sensitivity of endothelial cells in the heart (i.e. EdCs) are likely to be different from vascular endothelial cells and remain largely unknown. Calcium ion (Ca^{2+}) signaling is often associated with the direct cellular response to mechanical forces and initiates the mechanosensitive response in endothelial cells (*16*). Yet, how Ca^{2+} signaling leads to a cell specific response to mechanical forces remains unclear. Here, we examine the ability of mechanical forces to modulate specific endocardial fate towards valvulogenesis. We directly tested the signaling cascades activated by mechanical forces, quantitatively characterized their dynamic properties, and considered the implications of these observations for

transcriptional regulation of valve-specific markers *in vivo*. We find that valvular cell identity is directed by blood flow via two different mechanosensitive pathways: TRP mediated *klf2a* activation and ATP mediated Ca2+ oscillation leading to Nfatc1 signaling in response to local high shear stresses.

Using the zebrafish model system to allow for high precision control of spatiotemporal mechanical parameters (*17, 18*), we analyzed Ca^{2+} dynamic patterns via live imaging of the endocardium at cellular resolution. Ca^{2+} fluctuations are observed in many developmental contexts associated with tissue reorganization such as cell migration (*19*), wound healing (*20*), embryonic development, and regeneration (*21, 22*). In endothelial cells, Ca^{2+} fluxes have been shown to be involved in angiogenesis (*23, 24*). Thus, it is thought that Ca^{2+} is an important effector of cardiovascular morphogenesis. To address whether Ca^{2+} activation can be observed specifically in the EdCs, we expressed the fluorescent Ca^{2+} sensor protein GCaMP7a in endocardial/endothelial cells using a *Tg(fli1a:gal4ff);(uas:GCaMP7a)* system (*24*) along with *Tg(kdrl:nls-mCherry)*. We found that Ca^{2+} oscillations were observed almost exclusively in the EdCs of the atrioventricular canal (AVC) (Fig. 1, A to D, Fig. S1A and Movie S1) between 32 and 102 hpf (hours post fertilization). Normalization of the calcium signal obtained by computing the ratiometric intensity of GCaMP7a to nls-mCherry signals in tracked EdCs confirms that EdCs display Ca^{2+} oscillations (Fig. 1B and Movie S2). The occurrence of Ca^{2+} oscillations peaks at around 2.5 dpf and subsequently declines as the morphogenesis of functional valves proceeds (Fig. 1C). We found that around two thirds of EdCs in the AVC display Ca^{2+} oscillating at 54 hpf, and that this number decreases at later developmental stages (Fig. S1B). Similarly, the oscillation frequency reaches a maximum

at 54 hpf and declines at later stages (Fig. S1C). Interestingly, we found that the period of Ca^{2+} activation does not significantly vary with development stages even when the overall activity declines (Fig. S1D).

To verify that the calcium oscillations are associated with valvulogenic differentiation, we next searched for the decoder/effector of this Ca^{2+} signaling. Nuclear factor of activated T-cells (Nfatc1) is an established Ca^{2+} sensitive transcription factor known to control EndoMT and subsequent heart valve morphogenesis (*25-30*). The inactive form of Nfat is phosphorylated and sequestered in the cytoplasm. Nfatc1 activation is mediated by calcium via the calmodulin dependent serine/threonine protein phosphatase Calcineurin in response to Ca^{2+} (*43*). Upon the activation of Calcineurin, Nfat is de-phosphorylated and subsequently translocated to the nucleus to activate transcription (*30*, *31*). Nfatc1 is thus both a good marker of valve cell identity and a candidate for a relay protein decoding the levels of cytoplasmic Ca^{2+} to generate a transcriptional response. (Fig. S2A). We generated a Nfat binding element reporter line, *Tg(4xnfbr:d2EGFP)*, which expresses d2EGFP in response to the binding of nuclear-localized Nfat protein (Fig. S2B). Nfat reporter expression was observed in EdCs of the AVC from 34 hpf onward (Fig. 1, E and F, and Fig. S2C). At 78 hpf, the number of d2EGFP positive cells starts to decrease in the EdCs of AVC, but the reporter still displays a specific expression in EdCs in the AVC (Fig. 1E). Nfat reporter activation was thus strikingly similar to the time course observed for the Ca^{2+} response (Fig. 1, C and F). To confirm these results, we additionally tracked Nfat nuclear re-localization by generating an endothelial/endocardial-specific GFP-Nfatc1 reporter allowing to monitor Nfat subcellular distribution (Fig. S2F). As expected, we found that the GFP-Nfatc1

localisation varies in the endocardium with strong nuclear localization in the AVC while GFP-Nfatc1 remains cytoplasmic in the other cells of the endocardium (Fig. S2F). Together, these results highlight that both spatial and temporal regulation of Ca^{2+} signaling and Nfat activation are unique features of the EdCs located in the developing valve area during heart development, suggesting an important role during valve formation in response to mechanical forces.

Previous studies have shown that Ca^{2+} levels in EdCs are associated with changes in mechanical forces but Ca^{2+} dynamics in response to mechanical force changes have never been described (*4*). To test if the observed Ca^{2+} oscillations in EdCs are force-responsive, we first assessed the Ca^{2+} signals in hearts stopped using of MS-222 or p-amino blebbistatin treatment. We found that in these conditions, Ca^{2+} activation was abrogated in EdCs (Fig. S3, A to C). Importantly, Ca^{2+} oscillations recovered upon wash-out and restarting of the heartbeat (Fig. S3, A and B). Next, we assessed the impact of decreased flow forces associated with lower hematocrit by analyzing the *gata1a* mutant zebrafish line that do not have red blood cells (*32-34*). Lower hematocrit significantly affects shear stress and flow profile in the AVC (*35, 36*). Consistent with the heart-arrested condition, *gata1a* mutants (and *gata1a* morphants), exhibited a decreased number of Ca^{2+} spikes at both 54 hpf and 76 hpf (Fig. S3, D and E). We also found a significant decrease of Nfat activity in the *gata1a* mutants (Fig. S3F). Together, these results suggest that both Ca^{2+} oscillations and Nfat activation are stimulated in response to mechanical forces generated by the beating heart.

In the heart, cardiomyocytes have been proposed to activate EdC responses to forces,

131 suggesting that endocardial cells are not the direct force sensor (*37*). It is thus important
132 to confirm that mechanical forces are indeed directly leading to Ca^{2+} signaling in the
133 endocardium. Consequently, we set out to alter the mechanical force distribution in the
134 living heart by artificially changing the boundary conditions and thus the flow forces in
135 the system (Fig. 2A). To this end, we inserted single agarose-based magnetic beads into
136 the cardiac lumen by microsurgery using 30-60 μm diameter beads that can be inserted
137 in the atrium or the ventricle without completely blocking heart function and flow in the
138 beating heart (Fig. 2B and Movie S3). The presence of the bead in the heart alters the
139 flow forces generated in the beating heart. To quantify the flow generated around the bead,
140 we performed a 3D simulation of the wall shear stress and pressure around the bead using
141 image-based computational fluid dynamics simulation with a dynamic wall motion (*38*)
142 (Fig. 2C and Fig. S4, A to C). We found that both parameters are increased in the vicinity
143 of the bead, indicating an increase in the flow forces generated around the grafted bead
144 (Movie S4). Interestingly, the calculated wall shear stress amplitude generated by the
145 presence of the bead in the atrium (3 Pa) is close to the endogenous wall shear stress
146 amplitude generated in the AVC at 48 hpf where the valve normally forms (between 3
147 and 7 Pa) (*4, 38, 39*). *In vivo*, we analysed the Ca^{2+} response of the EdCs and found that
148 Ca^{2+} spikes were observed in the EdCs close to the bead when trapped in the atrium or in
149 the ventricle, whereas sham injected embryos never display any Ca^{2+} activation except in
150 the AVC (Fig. 2D, Fig. S4, D and E, and Movie S5 and S6). The Ca^{2+} activation period
151 lasted an average of 5.5 sec around beads in the EdCs of the atrium or the ventricle (Fig.
152 S4F).
153
154 To further demonstrate that the impact of shear stress directly affects the EdC calcium

response in live embryo, we directly manipulated the bead within the heart using magnetic tweezers. This approach permits to generate controlled shear forces in an immobilized heart (Fig. 2E). We first calibrated the velocity of the bead pulled by the magnetic tweezer and quantified the amount of force it can generate in the zebrafish heart (Fig. S4, G and H). We found that the force generated by the magnetic bead in motion ranged between 100 to 2000 pN, a stimulus which is slightly higher than endogenous wall shear stresses generated in the AVC (*4, 38, 39*). While the magnet probe alone did not affect Ca^{2+} influx in EdCs, direct pulling of the magnetic bead lead to the generation of Ca^{2+} influx in the EdCs of the arrested heart (Fig. 2, F to H, Fig. S4, I and J, and Movie S7). Together, these results indicate that Ca^{2+} fluxes are induced in the EdCs by mechanical forces such as wall shear stress and associated wall pressure.

We next assessed the biological relevance of the localized response initiated by bead grafting and tested the role of ectopic forces in the initiation of valve formation. Considering that bead grafting leads to the generation of a typical mechanosensitive response in ectopic areas of the heart, we addressed if it is associated with the formation of ectopic valves. Notably, 16-20 hours after bead grafting in the atrium, valve-like EdCs clusters were observed near the grafted beads. The valve like structures were visible in the atrial region that protruded from the atrial surface to the atrial cavity or the cardiac jelly, respectively (Fig. 3A). We found that both the activity of Nfat and Notch signaling, which are specific to valve cell identity (*40-42*), were strongly activated in the valve like EdCs cluster generated near the grafted bead (Fig. 3A and Fig. S5A). To confirm the results, we grafted a bead into atrial lumen at 50 hpf or 74 hpf and assessed the Nfat reporter activity as a response to increase forces. Four hours after bead grafting, Nfat

reporter response was ectopically activated in EdCs located near the bead (Fig. 3B and Fig. S5B). These results were consistent with the fact that Nfat activity is dramatically reduced when heart contractility is affected (Fig. S5, C and D). Conversely, we found that Nfatc1 nuclear localization is activated in response to ectopic forces (Fig. S5E). We could confirm that nuclear activity of nfatc1 is dependent on the ser/thr de-phosphorylation by using a chemical blocker of Calcineurin (FK506) (Fig. S5E). Thus, the nuclear localization of GFP-Nfatc1 is promoted by increased mechanical force, in a Nfatc1 ser/thr de-phosphorylation dependent manner.

To clarify the cell identities within the ectopic structures, we followed two different approaches. We first generated a BAC transgenic line using the well-established EndoMT marker *twist1b*, *TgBAC(twist1b:GFP)*, to highlight cells that underwent EndoMT in the valvuloids. We clearly found Twist1b positive cells undergoing EndoMT in the developing valve cushion and strong expression in the mesenchymal cells of the developing valve (Fig. S6, A to C). When ectopic forces generated by beads lead to valvuloid structures, Twist1b positive cells were populating the valve-like structure (Fig. 3C). We also observed that the grafted beads trigger the generation of mis-localised protrusions into cardiac jelly, which constitute the first sign of cardiac valve morphogenesis in zebrafish (*44*) (Fig. 3A). This observation along with the presence of Nfat and Notch positive cells indicate that the ectopic valve like structures have important similarities with endogenous valves.

To further confirm these observations, we next assessed if other valve related genes are induced in response to the presence of ectopic forces in the endocardial cells (Fig. S6, D

to H). Klf2 and Wnt9b have been shown to control heart valve remodeling in response to mechanical forces in mouse and zebrafish (*45*). Using RNAscope, we found that the grafted beads induced the ectopic expression of *klf2a* and *wnt9b* in the endocardial cells surrounding it. In addition, we found that *klf4a*, a known modulator of EndoMT in EC (*46*, *47*) was also activated in response to ectopic forces. Interestingly, both *klf2a* and *klf4a* expression were not affected when calcineurin was inhibited FK506, suggesting that Ca^{2+}-Nfat signaling pathway act independently of the *klf2a-wnt9b* mechano-transduction pathway. Conversely, *egr1*, a known mechanosensitive gene specifically expressed in the AVC (*48*), was downregulated by calcineurin inhibition (Fig. S6, I and J). This suggests that *egr1* acts downstream of Nfatc1. Thus, endocardial cells experiencing ectopic forces activate the morphogenetic program which is promoting the expression of valve remodeling and EndoMT markers required for the endogenous AV valve development. These results demonstrate that mechanical forces are key to specify heart valve position during development by modulating both the Klf2a-Wnt9b and the Nfatc1 signaling pathways.

Considering Nfat and Klf2a-Wnt9b seem to define two different mechanosensitive pathways, we next characterized the factors which are responsible for the force-dependent Ca^{2+} - Nfat signal activation. We first focused on stretch sensitive channel proteins (*3*, *4*) and primary cilia (*49*) because they have been widely implicated in flow sensing in the cardiovascular system (*3*, *50*). We used established mutant lines for the stretch sensitive channels Trpp2, Trpv4, Piezo1, Piezo2a and Piezo2b (*4*, *51*, *52*) and iguana (Dzip1) (*53*) which is responsible for ciliogenesis in the cardiovascular system (*54*). We found that all of these mutants showed normal Ca^{2+} activation (Fig. S7, A and B). These results were

confirmed by the fact that gadolinium ion (Gd^{3+}), a non-specific stretch-sensitive channel blocker, did not suppress the Ca^{2+} influx significantly (Fig. S7C). These results suggest that primary cilia and stretch sensitive channels are not the main regulators of the Ca^{2+} oscillations observed in EdCs.

Considering none of the expected stretch sensitive channels affected calcium oscillations, we turned to paracrine signals potentially released in response to mechanical forces. Previous studies have shown that Adenosine 5' triphosphate (ATP) is released in cultured endothelial cells in response to mechanical stimuli (*16*). As a response, ATP activates Ca^{2+} signaling via an increase of the permeability of cations in purinergic receptor P2X channels (*55*) (Fig. 4A). We thus hypothesized that intracellular Ca^{2+} fluxes are dependent on ATP levels. ATP can be generated by endothelial mitochondria (*56*). Accordingly, we found that the Ca^{2+} influx in EdCs of the AVC was abolished when cytosolic ATP levels are depleted by oligomycin A, a mitochondrial ATP synthase inhibitor (Fig. S7D). We next investigated whether extracellular ATP is able to alter Ca^{2+} influx in EdCs by microinjecting oligomycin A, apyrase (an ATPase) and ATPγS (an ATP analog) into the cardiac lumen (Fig. 4B, and Movie S8). After both oligomycin A and apyrase injection, we found that the Ca^{2+} influx was significantly suppressed in the EdCs of the AVC; conversely, ATPγS significantly increased the amount of Ca^{2+} influx (Fig. 4C, and Fig. S7, E to G). In addition, ATPγS led to a significant increase of both the number of cells displaying Ca^{2+} spikes and the Ca^{2+} oscillation frequency in the EdCs (Fig. S7, H and I). Importantly, the heart rate and the cell viability were not affected by these treatments, suggesting that none of them altered the mechanical forces associated with heart function. These results indicate that extracellular ATP is the trigger of Ca^{2+} signaling in EdCs in

response to flow.

The requirement of extracellular ATP for the Ca^{2+} influx in EdCs prompted us to investigate the involvement of known ATP dependent channels such as P2X channels that are activated by disturbed flows in response to ATP release in endothelial cells (*57, 58*). We first examined whether P2X (P2rx in zebrafish) channels are expressed in the EdCs. We found that *p2rx1*, *p2rx4a* and *p2rx7* transcripts are present in the endocardial cells of the heart at 48 hpf and 72 hpf (Fig. S8, A and B). Thus P2rx expression is not restricted to the AVC. Treatment against antagonists of P2X1, 4 and 7 decreased the number of Ca^{2+} spikes in the EdCs (Fig. S8C). In line with this result, the embryos overexpressed a dominant-negative form of either human *P2X4* (*hP2X4C353W*) or zebrafish *p2rx4a* (*zP2rx4aC365W*) mRNA, as well as *p2rx4a* morphants, displayed a significant decrease in the number of Ca^{2+} spikes in EdCs without affecting heartbeat (Fig. 4D, and Fig. S8, D to G, and I). Overall, these results show that the Ca^{2+} influx in EdCs is modulated by P2X channels in response to changes in extracellular ATP levels.

To understand how the activation and inhibition of P2X-mediated ATP signaling could affect valve formation, we first assessed how altering calcium oscillations translate into changes in gene expression. We tested whether P2X channels are involved in modulating Nfat activity in EdCs. Although embryos treated with combinations of P2X1, 4 and 7 antagonists, combinations of P2X4 with P2Y2 antagonists, P2X4 antagonist, or P2Y2 antagonist significantly suppressed the Nfat reporter activation, the other P2X/P2Y antagonists had no significant effect (Fig. S9, A and B). Furthermore, injection of a dominant-negative form of *p2rx4* mRNA significantly suppressed reporter expression (Fig. 4E and Fig. S8H), which correlates with abnormal Ca^{2+} activation (Fig. 4D and Fig.

S8G). Although Vegf signaling is known to activate Nfat signaling (*59*), Ki8751, a Vegfr2 inhibitor, had no effect on both Nfat reporter expression and Ca^{2+} activation in the EdCs (Fig. S9, A to D). Together, these results suggest that P2X and P2Y receptors coordinately modulate Nfat activity in the EdCs independently of VEGF signaling. In addition, we found that the Nfat activity in the endocardium seems unrelated to the tyrosine phosphorylation of Nfat determined by treatment of Janex-1 inhibiting jak3 which specifically phosphorylates Nfat tyrosine (Fig. S9, A and E).

We finally tested the valve phenotype in the embryos with suppressed extracellular ATP signaling. Although we found that Twist1b-positive cells localized in the endocardium, they were mis-localized when p2rx function was inhibited (Fig. 4F and Fig. S10, A and B). In addition, embryos displayed abnormal valve structures with incomplete morphogenesis of the valve and absence of leaflet formation (Fig. 4G). We additionally found that endocardial cells were excluded from the luminal part of the valve when Nfat activity is suppressed in these cells (Fig. S10, C and D). Altogether these results confirm that P2X functions acts upstream of Nfat activity to control EndoMT necessary for the valve development.

Mechanical forces have been implicated in a broad range of events during embryonic development (*60-62*). The presented work reframes our view of how endothelial cells interpret mechanical forces and supports the intriguing possibility that valve formation is mainly defined by the mechanosensitive inputs resulting from the local tissue constraints and flow forces (*26, 44, 63-65*). Piezo and Trp channels are well established stretch sensitive channels involved in cardiovascular morphogenesis and valve development through the Notch and *klf2a-Wnt9b* pathway (*4, 5, 51, 66, 67*). Our work identifies ATP

as an additional mechanosensitive paracrine signal by which hemodynamic forces can direct heart valve development, a compound that could be used to help grow heart valves *in vitro* and may be involved in congenital heart valve defects.

Figures and legends

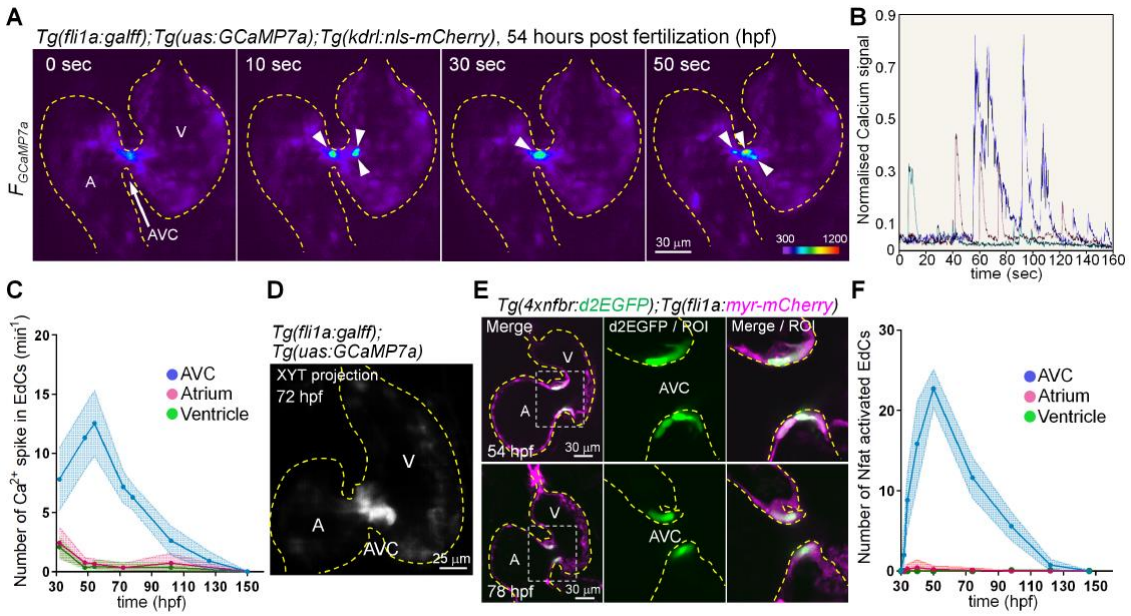

Fukui H et al., Fig. 1

Fig. 1. Endogenous Ca^{2+} influx and Nfat signal activation occur in EdCs of the AVC during heart valve development. (**A**) Representative single-scan beating heart images of the *Tg(fli1a:galff);Tg(uas:GCaMP7a);Tg(kdrl:nls-mCherry)* embryo at 54 hpf. Panels indicate the heat map-colored GCaMP7a images at indicated time points. Arrowheads and dashed lines indicate the activated GCaMP7a signal in the EdCs and the outline of the endocardium, respectively. (**B**) Normalized Ca^{2+} dynamics determined by $F_{GCaMP7a}/F_{nls\text{-}mCherry}$ in selected images that correspond to the same point of the cardiac cycle. Each color lines indicate the ratiometric change of individual cells (three cells). (**C**) The number of Ca^{2+} spike in EdCs of the atrium (red), ventricle (green) and AVC (blue) from 32 hpf to 150 hpf (n > 5). (**D**) XYT projection of GCaMP7a signal at 72 hpf in the same excitation position heart images for 60 sec (20 images). (**E**) Confocal single-scanned heart images of *Tg(4xnfbr:d2EGFP);Tg(fli1a:myr-mCherry)* embryo at 54 hpf (top panels, n = 20) and 78 hpf (bottom panels, n = 12). (**F**) The number of Nfat reporter

activated EdCs in the atrium (red), ventricle (green) and AVC (blue) from 30 hpf to 146 hpf (n = 12). In the following graphs, A, V and AVC indicate the atrium, ventricle, and atrio-ventricular canal, respectively. Images were taken ventral view and anterior to the top unless otherwise described.

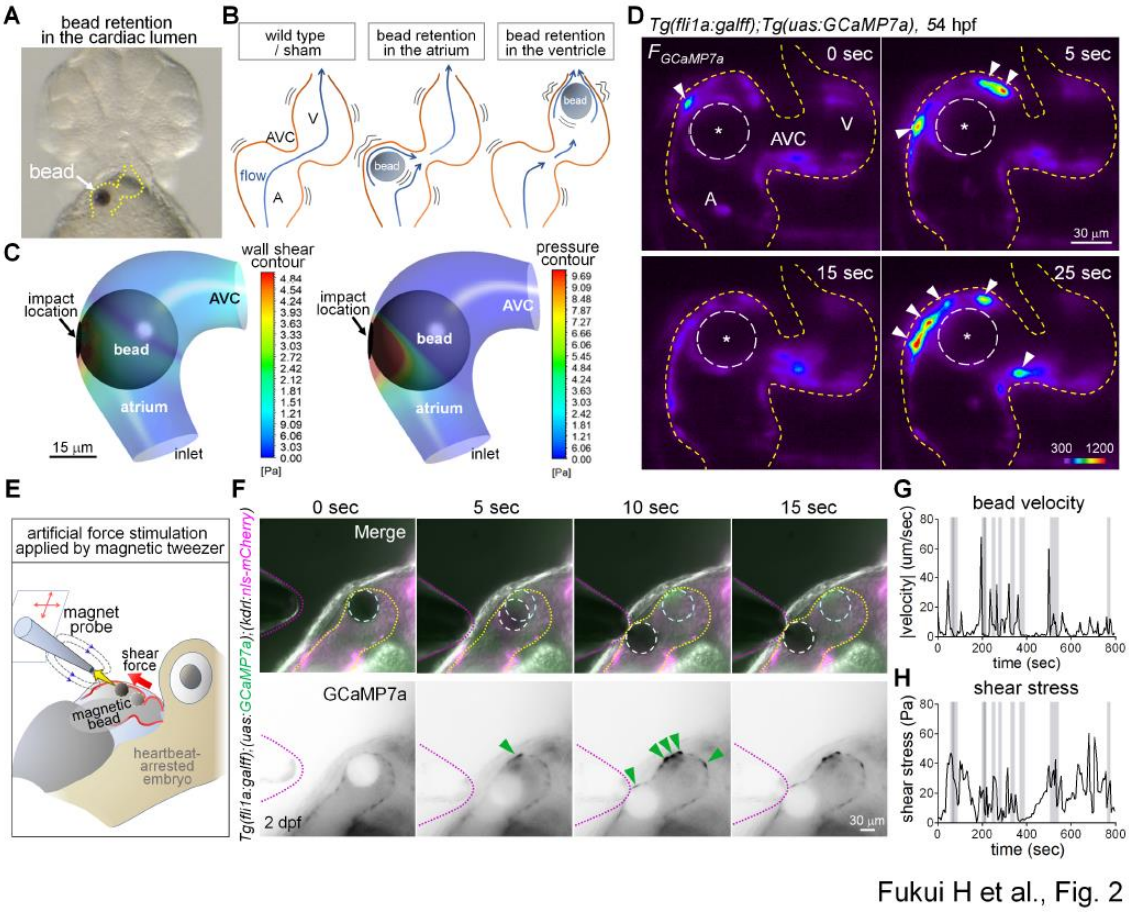

Fukui H et al., Fig. 2

Fig. 2. Force directly triggers Ca^{2+} influx in EdCs of zebrafish heart. (**A**) Representative image of bead implantation into the heart. Yellow dotted lines depict the outline of the heart. (**B**) Schematics of bead retention. (**C**) 3D simulation of wall shear stress (left) and pressure (right) in when the bead is close to the impact location. Force intensities are indicated by color. Clear circles indicate a bead. (**D**) Representative beating heart images of the embryo grafted with a bead (dashed circle with asterisk) at 54 hpf.

Arrowheads and yellow dashed lines indicate the GCaMP7a signal in the EdCs and the outline of endocardium, respectively. (**E**) Schematic of magnetic tweezer-based force application to a zebrafish heart. (**F**) Representative single-scan images of arrested heart of a *Tg(fli1a:galff);Tg(uas:GCaMP7a);Tg(kdrl:nls-mCherry)* embryo grafted with a magnetic bead (dashed white circle; the original position is depicted as a dashed cyan circle) pulled by the magnetic probe (dotted magenta lines) at 2 dpf. Green arrowheads and dotted yellow lines indicate the GCaMP7a signal in EdCs and the outline of endocardium, respectively. Images are left view of the embryo (N = 3, yielding similar results). (**G**), (**H**) Quantification of bead velocity (G) and shear stress (H) applied by the magnetic tweezer shown in movie S7. The grey shades represent the period of activated GCaMP7a signal in EdCs.

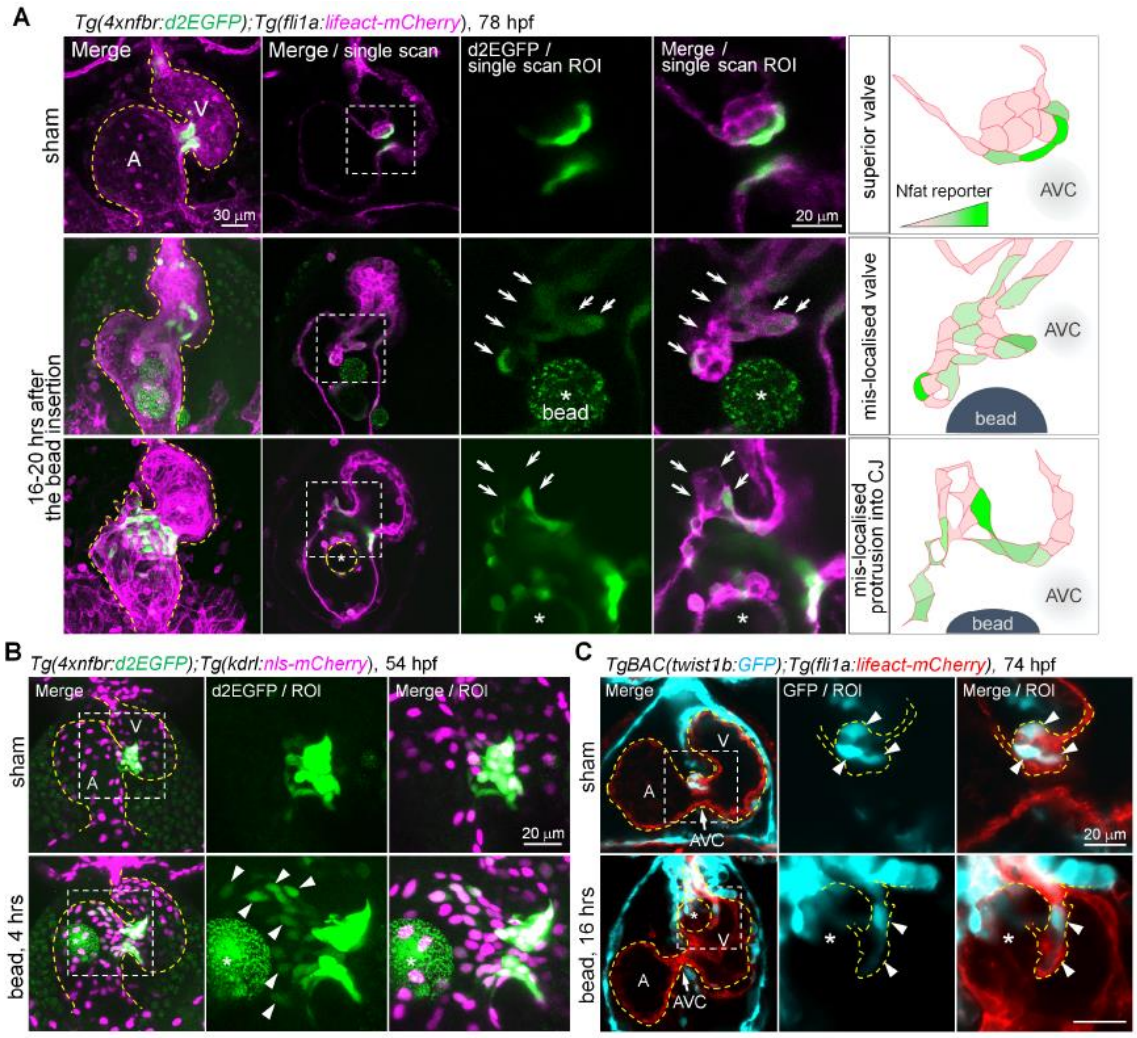

Fukui H et al., Fig. 3

Fig. 3. Artificial forces lead to the formation of valve like structures. (**A**) Representative confocal images of *Tg(4xnfbr:d2EGFP);Tg(fli1a:lifeact-mCherry)* embryo in sham-treatment (n = 11) and in 16-20 hours after retention of bead at 78 hpf (n = 8). The most-right panels indicate the schematics of superior valve (top), mis-localised valve (middle) and mis-localised protrusion into cardiac jelly (bottom row, arrowheads) with Nfat reporter intensity (N > 5, yielding similar results individually). Arrows indicate the ectopic structure induced by bead manipulation. (**B**) Representative confocal images (54 hpf) of *Tg(4xnfbr:d2EGFP);Tg(kdrl:nls-mCherry)* embryo in 4 hours after sham-treatment (n = 7) or bead grafting (n = 13). The experiment was performed independently

four-times, yielding to similar results. Arrowheads indicate the ectopic expression of Nfat reporter in EdCs. (**C**) Representative confocal images of *TgBAC(twist1b:GFP);Tg(fli1a:lifeact-mCherry)* embryo in sham-treatment (n = 10) and in 16 hours after retention of bead at 74 hpf (n = 7). Arrowheads indicate the Twist1b expression in EdCs. Yellow dashed lines depict the outline of the endocardium and demonstrating that superior valve in top panels and ectopic valve in bottom panels. Asterisks and dashed circles indicate the grafted bead in the heart lumen.

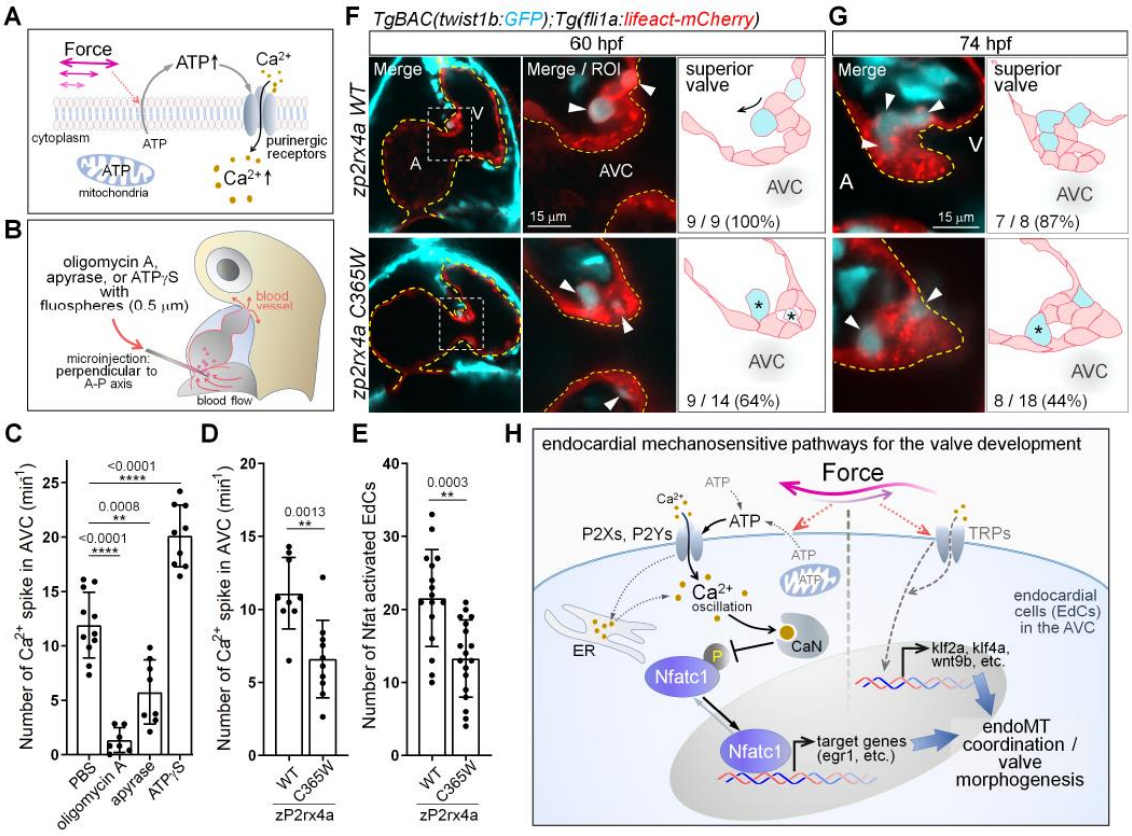

Fukui H et al., Fig. 4

Fig. 4. Extracellular ATP and P2rx channels function proper valve development. (**A**) Schematic of Ca^{2+} influx via extracellular ATP-dependent P2XRs activation. (**B**) Schematic of microinjection into cardiac lumen. (**C**) The number of Ca^{2+} spikes in EdCs

of the AVC for PBS (n = 11), oligomycin A (n = 7) apyrase (n = 8) and ATPγS (n = 9) injected embryos at 54 hpf. (**D**), (**E**) The number of Ca^{2+} influxes (D) and Nfat reporter activation (E) in EdCs of the AVC for embryos injected with *zp2rx4aWT* (n = 9 in [D]; n = 16 in [E]) and *zp2rx4aC365W* mRNA (n = 10 in [D]; n = 18 in [E]) at 54 hpf. (**F**), (**G**) Representative confocal images of *TgBAC(twist1b:GFP);Tg(fli1a:lifeact-mCherry)* embryo injected with *zp2rx4aWT* (n = 9 in [F]; n = 8 in [G]) and *zp2rx4aC365W* mRNA (n = 14 in [F]; n = 16 in [G]) at indicated time points. Arrowheads indicate the Twist1b expression in the EdCs. Yellow dashed lines as the outline of the endocardium and schematics of the superior valve in the right panels. Asterisks indicate the EdCs with an ectopic Twist1b expression that protruded from incorrect region. Arrow indicate cell movements to the cardiac jelly. (**H**) Schematic of endocardial mechanosensitive signal pathways for the valve development. Note that force triggers (ATP)-transducer (Ca^{2+})-decoder (NFAT) system which is independent of the klf2a/klf4a transcription activation.

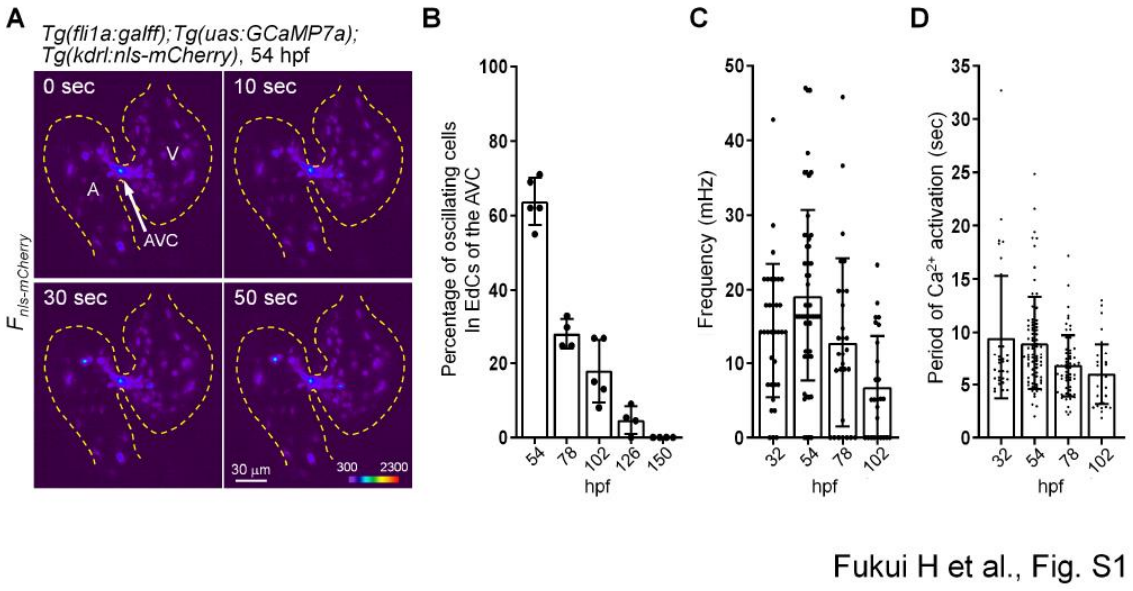

Fukui H et al., Fig. S1

Fig. S1. Characterization of Ca^{2+} influx in EdCs during heart valve development.

(**A**) Representative single-scan beating heart images of the *Tg(fli1a:galff);Tg(uas:GCaMP7a);Tg(kdrl:nls-mCherry)* embryo at 54 hpf. Panels indicate the heat map-colored nls-mCherry images at indicated time points. Yellow dashed lines indicate the outline of the endocardium. (**B**) Quantification of the percentage of Ca^{2+} oscillating cells in EdCs of the AVC at indicated time points: 54 hpf, n =5; 78 hpf, n = 4; 102 hpf, n = 5; 126 hpf, n = 4; 150 hpf, n = 4. (**C**) Frequency of Ca^{2+} spikes at several time points: 32 hpf, n = 34; 54 hpf, n = 56; 78 hpf, n = 29; 102 hpf, n = 29. (**D**) Quantification of the Ca^{2+} signal action period at several time points: 32 hpf, n = 45; 54 hpf, n = 77; 78 hpf, n = 62; 102 hpf, n = 37. In the following graphs, A, V and AVC indicate the atrium, ventricle, and atrio-ventricular canal, respectively. Images were taken from ventral view and anterior to the top unless otherwise indicated.

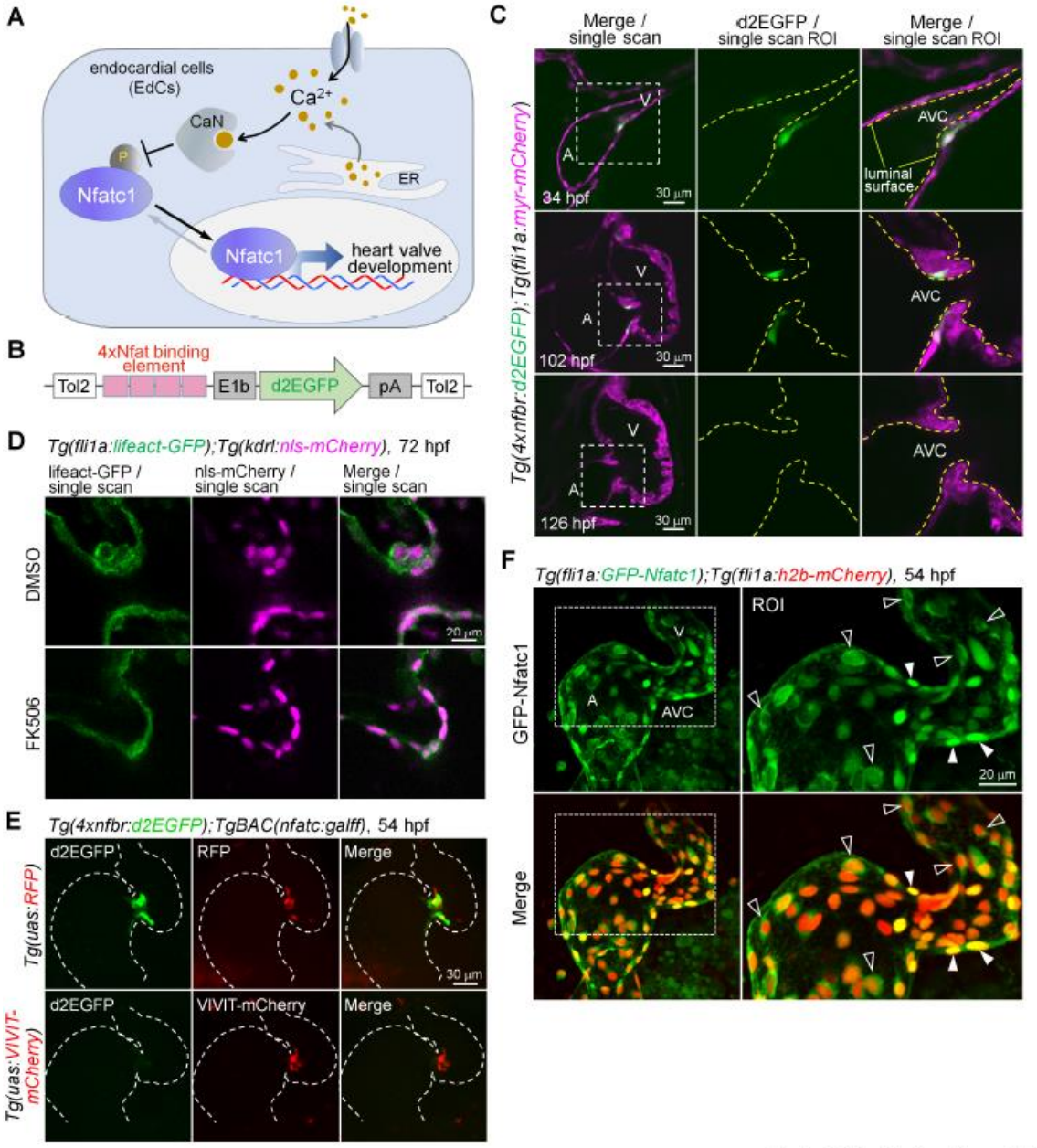

Fukui H et al., Fig. S2

Fig. S2. Characterization of Nfat reporter during heart valve development. (**A**) Schematic of Nfat signal activation via Ca^{2+} influx in EdCs. (**B**) Schematic of the reporter construct for monitoring Nfat signal activation. (**C**) Representative heart images of *Tg(4xnfbr:d2EGFP);Tg(fli1a:myr-mCherry)* embryo at 34 hpf, 102 hpf and 126 hpf (n = 14). Yellow dashed lines indicate the luminal surface of the EdC layer. (**D**) AVC region of *Tg(fli1a:lifeact-GFP);Tg(kdrl:nls-mCherry)* embryo at 72 hpf treated with DMSO (n

399 = 6) or FK506 (n = 6). Note that FK506 treatment blocks EdC migration into cardiac jelly
400 in the AVC. (**E**) Representative embryonic heart images of
401 *Tg(4xnfbr:d2EGFP);TgBAC(nfatc1:galff)* crossed with *Tg(uas:RFP)* (n = 8) or
402 *Tg(uas:VIVIT-mCherry)* (n = 11) at 54 hpf. Note that VIVIT-mCherry suppresses
403 d2EGFP expression. The experiment was performed independently three times, each
404 yielding similar results. (**F**) Representative confocal scanned 3D stack images of 54 hpf
405 *Tg(fli1a:GFP-Nfatc1);Tg(fli1a:h2b-mCherry)* embryonic heart (n = 7). Closed
406 arrowheads and open arrowheads indicate the representative nuclear- and cytoplasmic -
407 localised GFP-Nfatc1, respectively. The experiment was performed independently three-
408 times, each yielding similar results.
409

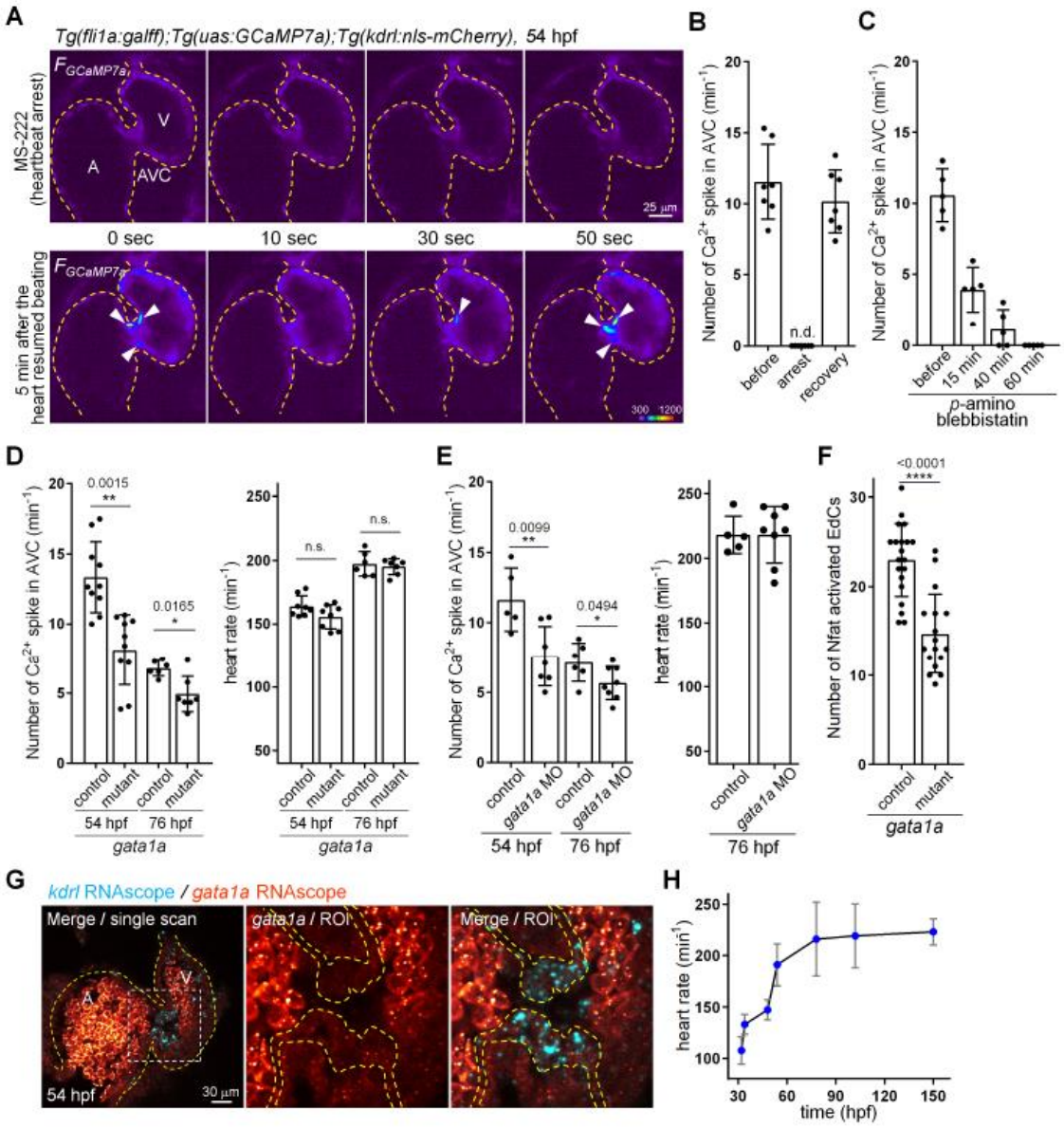

Fukui H et al., Fig. S3

Fig. S3. Heartbeat and fluid shear forces control the Ca^{2+} influx in EdCs of the AVC.

(**A**) Representative single-scan heart images of the *Tg(fli1a:galff);Tg(uas:GCaMP7a);Tg(kdrl:nls-mCherry)* embryo in a heart arrest condition by treatment with MS-222 (top panels) and in 5 min after heart resumed beating by wash-out of MS-222 (bottom panels) at 54 hpf. Panels indicate the heat map-colored GCaMP7a images at indicated time points. Arrowheads and dashed lines indicate the

activated GCaMP7a signal in the EdCs and the outline of endocardium, respectively. **(B)** The number of Ca^{2+} spikes in EdCs of the AVC at 54 hpf. GCaMP7a signals were imaged before heart arrest, during heart arrest by treatment of MS-222 (tricaine), and 5 min after the heart resumes beating (n = 7). (**C**) Quantitative analyses of the number of Ca^{2+} spike at the indicated time after the treatment of p-amino-blebbistatin at 54 hpf (n = 5). (**D**) The number of Ca^{2+} spikes in EdCs of the AVC (left) and the heartrate (right) of *gata1* mutant embryos at 54 hpf and 76 hpf. Control embryos (54 hpf, n = 10; 76 hpf, n = 6) and *gata1* mutant embryos (54 hpf, n = 10; 76 hpf, n = 7) were determined by presence or absence of blood cell circulation. (**E**) Quantitative analyses of the number of Ca^{2+} spikes in EdCs of the AVC at 54 hpf and 76 hpf (left) and heart rate at 76 hpf (right) of embryos injected with *control* MO (54 hpf, n = 5; 76 hpf, n = 6) or *gata1* MO (54 hpf, n = 7; 76 hpf, n = 8). (**F**) Quantitative analyses of the number of Nfat activated EdCs in *gata1* mutant embryos at 54 hpf (control, n = 20; mutant, n = 17). (**G**) Representative images of RNAscope analyses using *kdrl* with *gata1a* probes in 54 hpf embryos (n = 6). Dashed line in the single scan images and the ROI images indicate the outline of the heart and the endocardium, respectively. The experiment was performed independently twice, yielding similar results. (**H**) Quantitative analyses of the heart rate from 32 hpf to 150 hpf (n = 5).

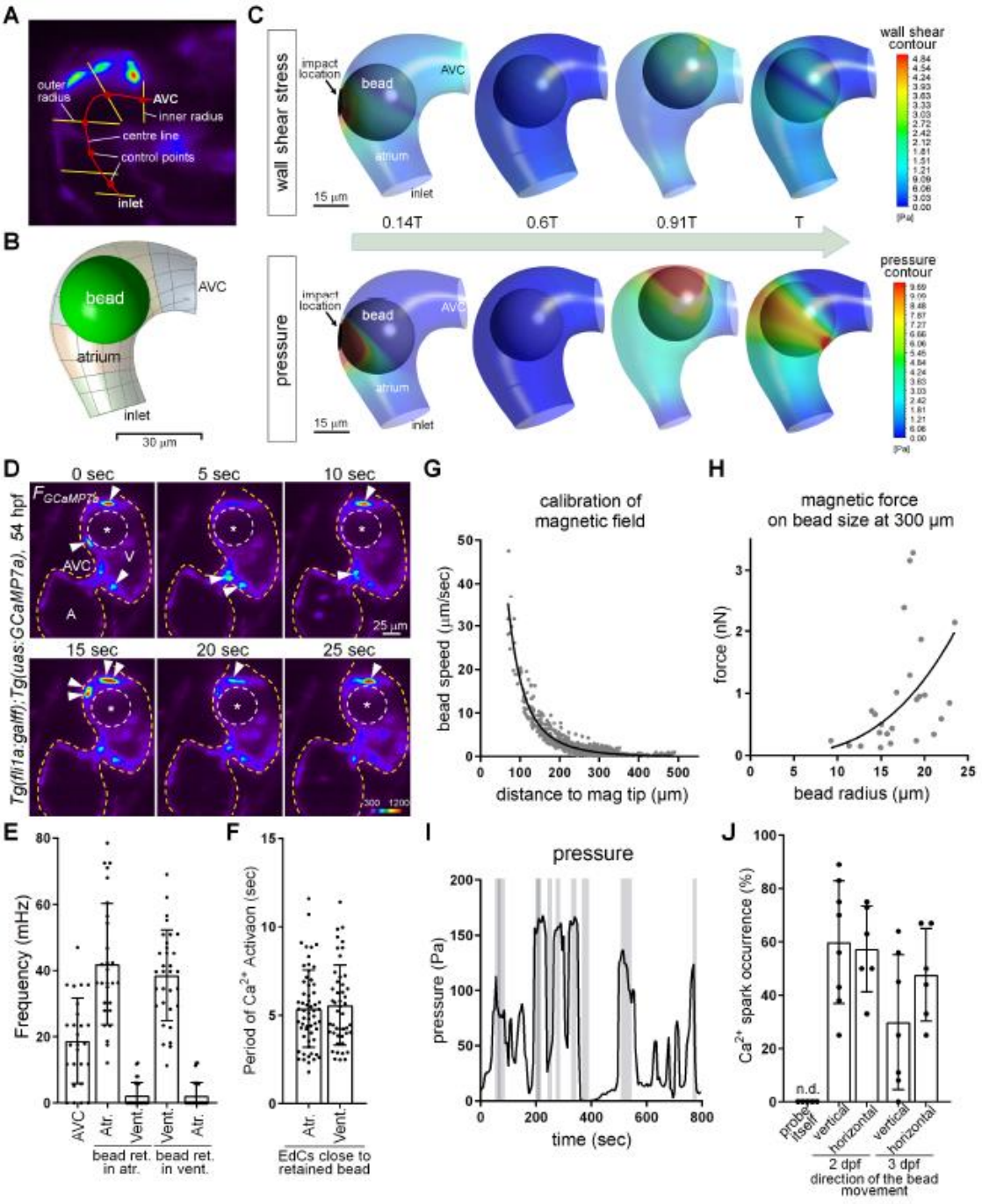

Fukui H et al., Fig. S4

Fig. S4. Retention of a bead in the cardiac lumen exerts forces on EdCs. (**A**) ~~Estimated 3D reconstruction of atrial chamber and magnetic bead for the simulation.~~ (**B**) ~~Motion waveform of the magnetic bead obtained from the video, plotted in normalized distance (X-coord) and cardiac cycle duration (T).~~ (**C**) 3D simulation of wall shear stress

(top panels) and pressure (bottom panels) in the bead manipulated in the atrium. Force intensities are shown in the heat map color. Clear circles indicate a 30 μm bead. (**D**) Representative single-scan beating heart images of the embryo retained with magnetic bead (dashed circle with asterisk) into ventricular lumen at 54 hpf. Panels indicate the heatmap-colored GCaMP7a images at the indicated time points. Arrowheads and yellow dashed lines depict the activated GCaMP7a signal in EdCs and the outline of endocardium, respectively. (**E**) Quantitative analyses for the frequency of Ca^{2+} oscillation in sham EdCs of the AVC (n = 26), EdCs close to grafted bead (atrium, n = 28; ventricle, n = 32) and EdCs of the other chamber which does not have a bead (atrium, n = 28; ventricle, n = 30). (**F**) Quantitative analyses for the period of Ca^{2+} activation in EdCs close to retained bead in the atrium (n = 59) or the ventricle (n = 47). (**G**) Calibration of magnetic field. Plot of the velocity with the distance between bead and magnet tip calculated by using 2.8 μm bead. (**H**) Magnetic force calibration on bead size at 300 μm distance. (**I**) Quantification of the pressure into EdCs applied by the magnetic tweezer shown in movie S7. The grey shades represent the period of activated GCaMP7a signal in EdCs. (**J**) Quantitative analyses of the ratio of Ca^{2+} spark occurrence in EdCs triggered by the magnetic tweezer. The direction of bead movement against the EdCs layer was classified as vertically (2 dpf, n = 8; 3 dpf, n = 7) and horizontally (2 dpf, n = 6; 3 dpf, n = 6). Note that pushing by the tip of the magnetic probe itself comes from the outside of the embryos was not triggered the Ca^{2+} spark in EdCs (n = 5).

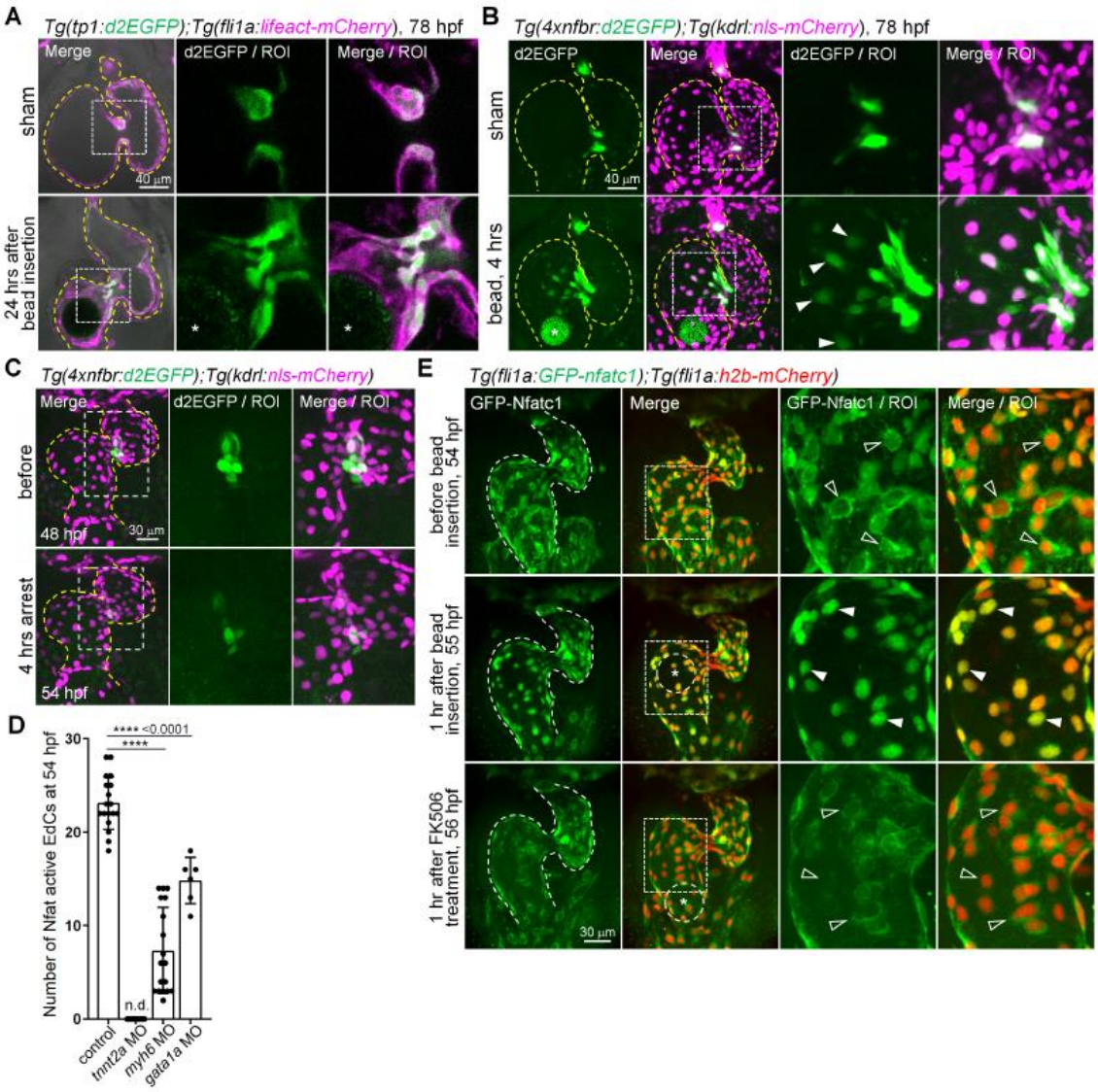

Fukui H et al., Fig. S5

Fig. S5. Bead retention leads to the ectopic reporter activation. (**A**) Representative single scanned confocal images of 78 hpf *Tg(tp1:d2EGFP);Tg(fli1a:lifeact-mCherry)* embryonic heart in 24 hours after sham-treatment (n = 6) and bead grafting (n = 3). The experiment was performed independently twice, each yielding similar results. (**B**) Representative confocal scanned 3D stack images of 78 hpf *Tg(4xnfbr:d2EGFP);Tg(kdrl:nls-mCherry)* embryonic heart in 4 hours after sham-treatment (n = 12) and bead grafting (n = 8). Arrowheads depict the activated Nfat reporter

in EdCs. The experiment was performed independently four-times, each yielding similar results. (**C**) Representative confocal images of *Tg(4xnfbr:d2EGFP);Tg(kdrl:nls-mCherry)* embryonic heart at 48 hpf (top panels, n = 5) and the same embryo after heartbeat has been arrested using BDM for 4 hours (bottom panels, n = 5). The experiment was performed twice yielding similar results. (**D**) Number of Nfat reporter activated EdCs at 54 hpf in embryos injected with *control* MO (control, n = 7), *tnnt2a* MO (n = 10), *myh6* MO (n = 18) and *gata1a* MO (n = 6). (**E**) Representative confocal scanned 3D stack heart images of *Tg(fli1a:GFP-Nfatc1);Tg(fli1a:h2b-mCherry)* before bead insertion (top panels, 54 hpf), with bead insertion for 1 hr (middle panels, 55 hpf), and 1 hr after FK506 treatment (bottom panels, 56 hpf) in the same embryos (n = 7). Closed arrowheads and open arrowheads indicate the representative nuclear- and cytoplasmic-localised GFP-Nfatc1, respectively. The experiment was performed independently three-times, each yielding similar results. Yellow dashed lines indicate the outline of endocardium.

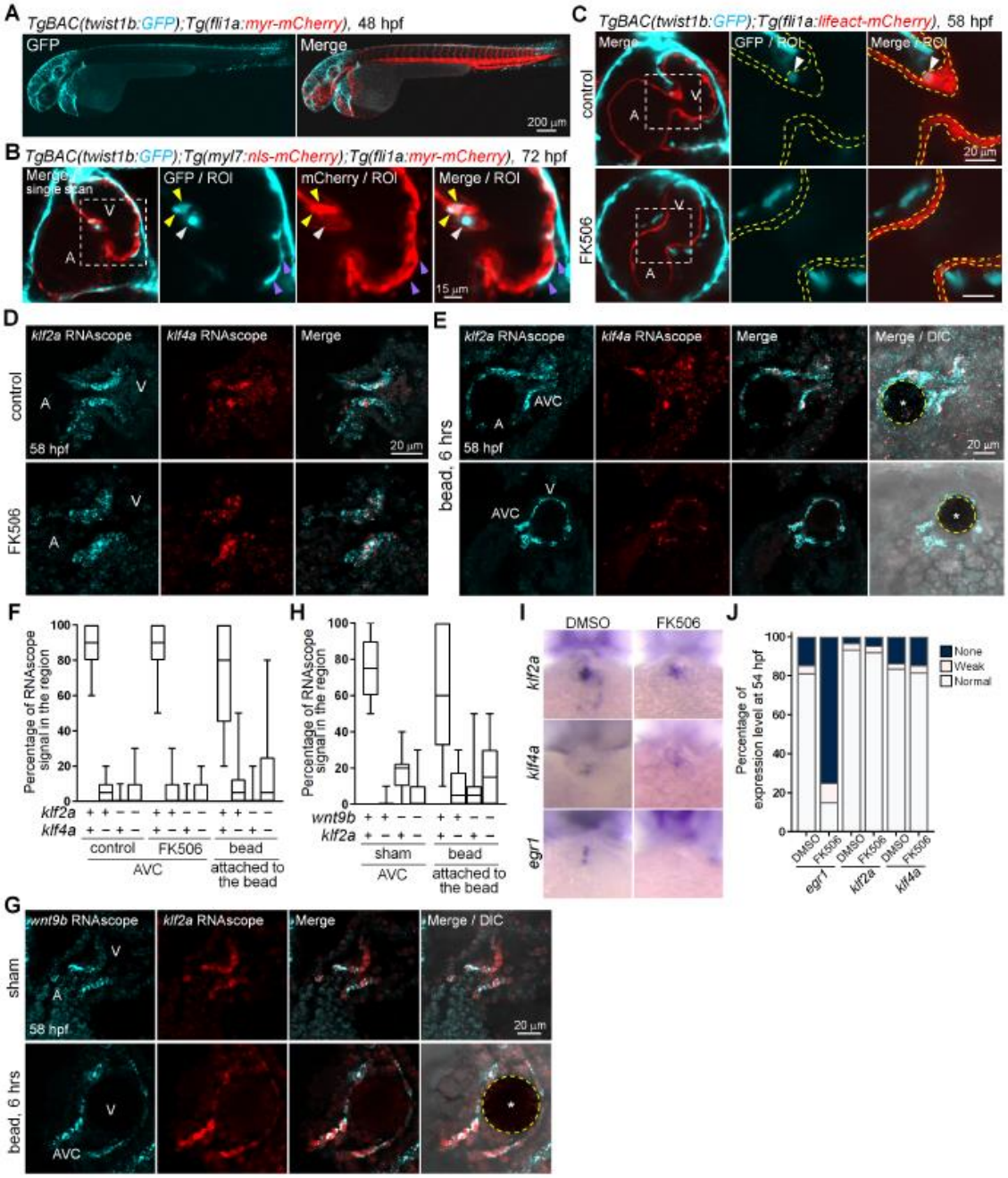

Fukui H et al., Fig. S7

Fig. S6. Nfat activation is dispensable for the force-dependent *klf2a/klf4a* expression. (**A**) Representative 3D stack confocal images of *TgBAC(twist1b:GFP);Tg(fli1a:myr-mCherry)* embryo at 48 hpf. Anterior to the left (n = 3). (**B**) Representative single scanned confocal heart images of *TgBAC(twist1b:GFP);Tg(myl7:nls-mCherry);Tg(fli1a:myr-mCherry)* embryo at 72 hpf. White arrowheads, yellow arrowheads, and purple

arrowheads indicate the Twist1b positive cells in the endocardium, myocardium, and epicardium, respectively (n = 4). (**C**) Representative single scanned confocal heart images of *TgBAC(twist1b:GFP); Tg(fli1a:lifeact-mCherry)* embryo treated with DMSO (control shown on top panels, n = 6) or FK506 (bottom panels, n = 6) at 58 hpf. Arrowheads and yellow dashed lines indicate the Twist1b positive cell and the outline of endocardium, respectively. The experiment was performed independently three-times, each yielding similar results. (**D**), (**E**) Representative images of RNAscope analyses of 58 hpf embryos treated with DMSO (control, n = 12, [D]), FK506 (n = 19, [D]) and bead insertion for 6 hrs (n = 13, [E]) using the *klf2a* with *klf4a* probes. (**F**), (**H**) Boxplot representing the ratio of positive RNAscope signal in selected 10 voxels (5 μm each) of the AVC (D in F; G in H) and of the EdCs attached to the bead (E in F; G in H). (**G**) Representative images of RNAscope analyses of 58 hpf embryos with sham treatment (n = 14), and bead insertion for 6 hrs (n = 17) using the *klf2a* with *wnt9b* probes. Yellow dashed circles with asterisk indicate the inserted bead in the cardiac lumen. (**I**), (**J**) Representative WISH images of 54 hpf embryos treated with DMSO or FK506 from 34 hpf to 54 hpf (I) and percentage of expression level categorized for three patterns (normal, weak and none) (J). Following anti-sense probes were used: *klf2a*, n = 122 (DMSO) and n = 127 (FK506); *klf4a*, n = 73 (DMSO) and n = 55 (FK506); *egr1*, n = 123 (DMSO) and n = 151 (FK506). The experiment was performed independently four times, yielding similar results.

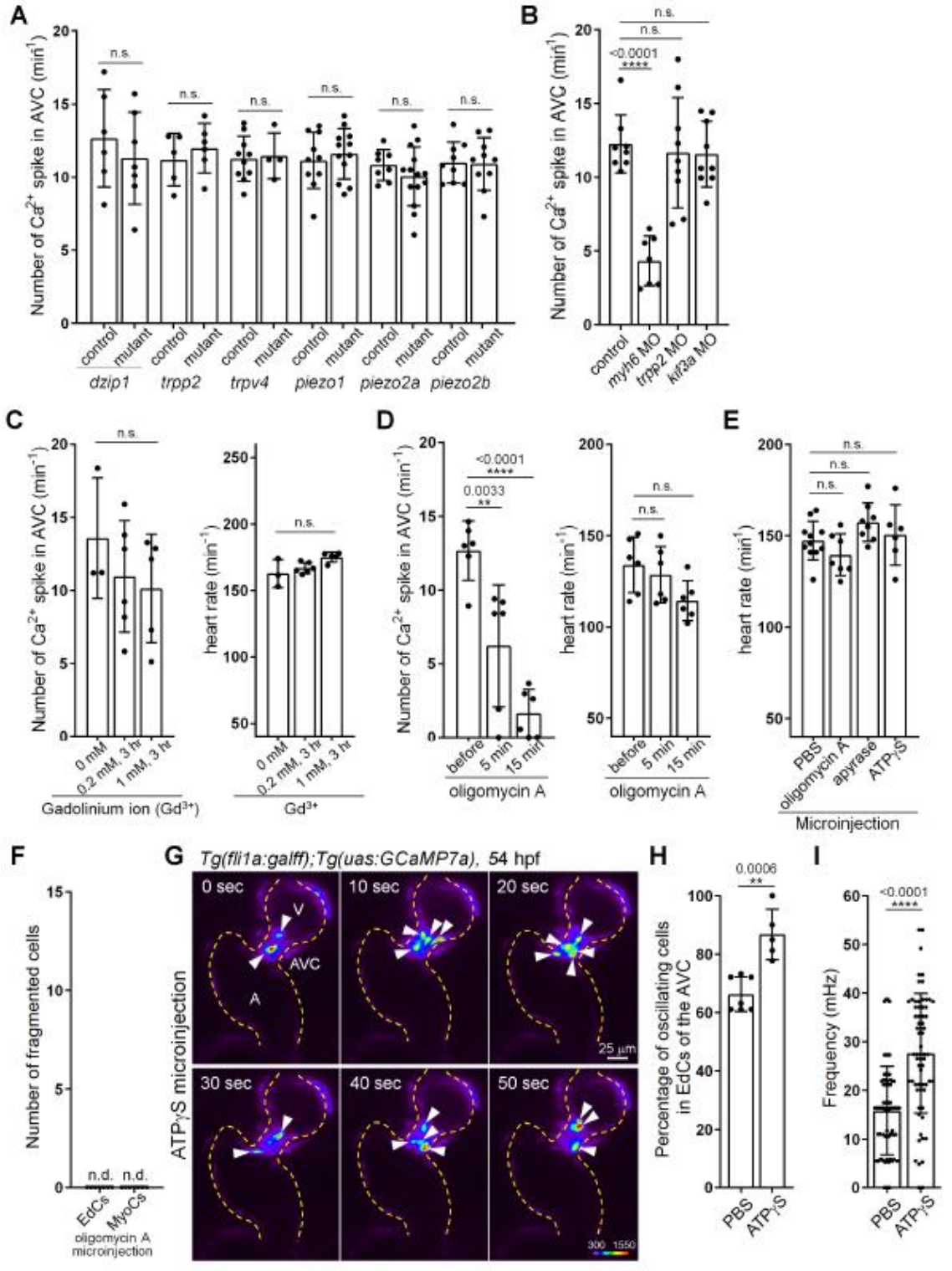

Fukui H et al., Fig. S8

509

510 **Fig. S7. Ca^{2+} influx in EdCs is regulated by extracellular ATP-dependent signaling.**

(**A**) Quantitative analyses of the number of Ca^{2+} spikes in EdCs of the AVC of *dzip1, trpp2, trpv4, piezo1, piezo2a and piezo2b* mutant embryos at 54 hpf. Control embryos represent the wild type and heterozygous embryos (*dzip1* control, n = 6; *dzip1* mutant, n = 7; *trpp2* control, n = 5; *trpp2* mutant, n = 6; *trpv4* control, n = 10; *trpv4* mutant, n = 4; *piezo1* control, n = 10; *piezo1* mutant, n =12; *piezo2a* control, n = 8; *piezo2a* mutant, n = 14; *piezo2b* control, n = 9; *piezo2b* mutant, n = 10). (**B**) Quantitative analyses of the number of Ca^{2+} spikes in EdCs of the AVC in embryos injected with *control* MO (n = 8), *myh6* MO (n = 7), *trpp2* MO (n = 9) and *kif3a* MO (n = 9). (**C**) Quantitative analyses of the number of Ca^{2+} spike in EdCs of the AVC (left) and heart rate (right) in embryos treated with 0.2 mM (n = 6) and 1 mM (n = 5) $GdCl_3$ at 54 hpf (No treatment indicated as 0 mM, n = 3). (**D**) The number of Ca^{2+} spikes in EdCs of the AVC (left) and heart rate (right) at 54 hpf (n = 6) before, 5 min after, and 15 min after oligomycin A treatment. (**E**) Quantitative analyses of the heart rate in for PBS (n= 11), oligomycin A (n = 7), apyrase (n = 8) and ATPγS (n = 6) injected embryos at 54 hpf. (**F**) The number of fragmented EdCs and MyoCs in embryos injected with oligomycin A (n = 7). (**G**) Representative beating heart images of an embryo microinjected with ATPγS at 54 hpf. Panels indicate the heat map-colored GCaMP7a images at indicated time points. Arrowheads and dashed lines depict the activated GcaMP7a signal in EdCs and the outline of the endocardium, respectively. (**H**), (**I**) Quantitative analyses of the percentage of Ca^{2+} oscillating cells in EdCs of the AVC (PBS, n = 7; ATPγS, n = 5) (H) and the frequency of Ca^{2+} spikes (PBS, n = 71; ATPγS, n = 66) (I) in embryos injected with PBS or ATPγS at 54 hpf.

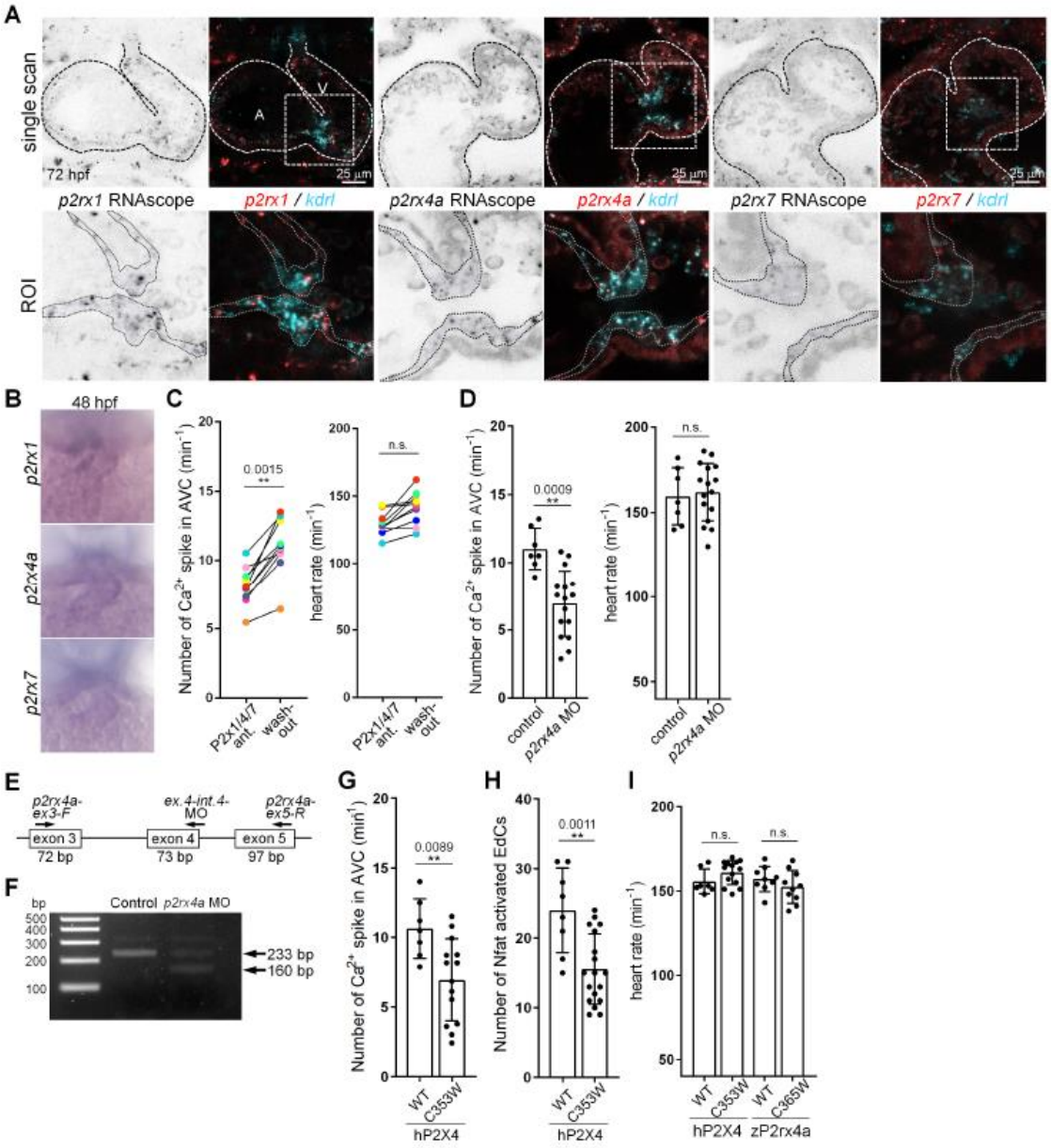

Fukui H et al., Fig. S9

Fig. S8. Ca^{2+} influx and Nfat reporter activation are regulated by P2rx channels expressed in EdCs. (**A**) Representative images of RNAscope analyses of 72 hpf embryos using the following RNAscope probes: *kdrl* with *p2rx1*, n = 10; *kdrl* with *p2rx4a*, n = 12; *kdrl* with *p2rx7*, n = 7. Dashed line in single scan images and the region between the dotted lines in ROI images indicate the outline of the endocardium and the endocardium, respectively. The experiment was performed independently twice, yielding similar results.

(**B**) Representative images of WISH analysis of 48 hpf embryos using the following anti-sense probes: *p2rx1*, n = 20; *p2rx4a*, n = 24; *p2rx7*, n = 18. The experiment was performed independently three times, yielding similar results. (**C**) The number of Ca^{2+} influxes in EdCs of the AVC (left) and heart rate (right) for 60 min of each 10 μM of p2rx1_4_7 antagonists (NF023, 5-BDBD and A438079) treated embryos and wash-out embryos at 54 hpf embryos (n = 10). (**D**) Quantitative analyses of the number of Ca^{2+} spikes in EdCs of the AVC (left) and heart rate (right) in embryos injected with *control* MO (n = 7) or *p2rx4a* MO (n = 16) at 54 hpf. (**E**) Schematic of primer set and MO target site of *p2rx4a*. (**F**) RT-PCR analysis to reveal the splicing-block by *p2rx4a* MO. Total RNA from embryos injected with MOs at 48 hpf were collected and subjected RT-PCR. Note that the samples injected with *p2rx4a* MO show the 160 bp band that is skipped in exon 4 of *p2rx4a*. (**G**), (**H**) The number of Ca^{2+} influxes (G) and Nfat reporter activation (H) in EdCs of the AVC for embryos injected with *hP2X4 WT* (n = 7 in [G]; n = 8 in [H]) and *hP2X4C353W* (n = 14 in [G]; n = 18 in [H]) mRNA at 54 hpf. (**I**) Quantitative analyses of the heart rate in embryos injected with *hP2X4 WT* (n = 7), *hP2X4C353W* (n = 14), *zp2rx4aWT* (n = 9) and *zp2rx4aC365W* (n = 10) mRNAs at 54 hpf.

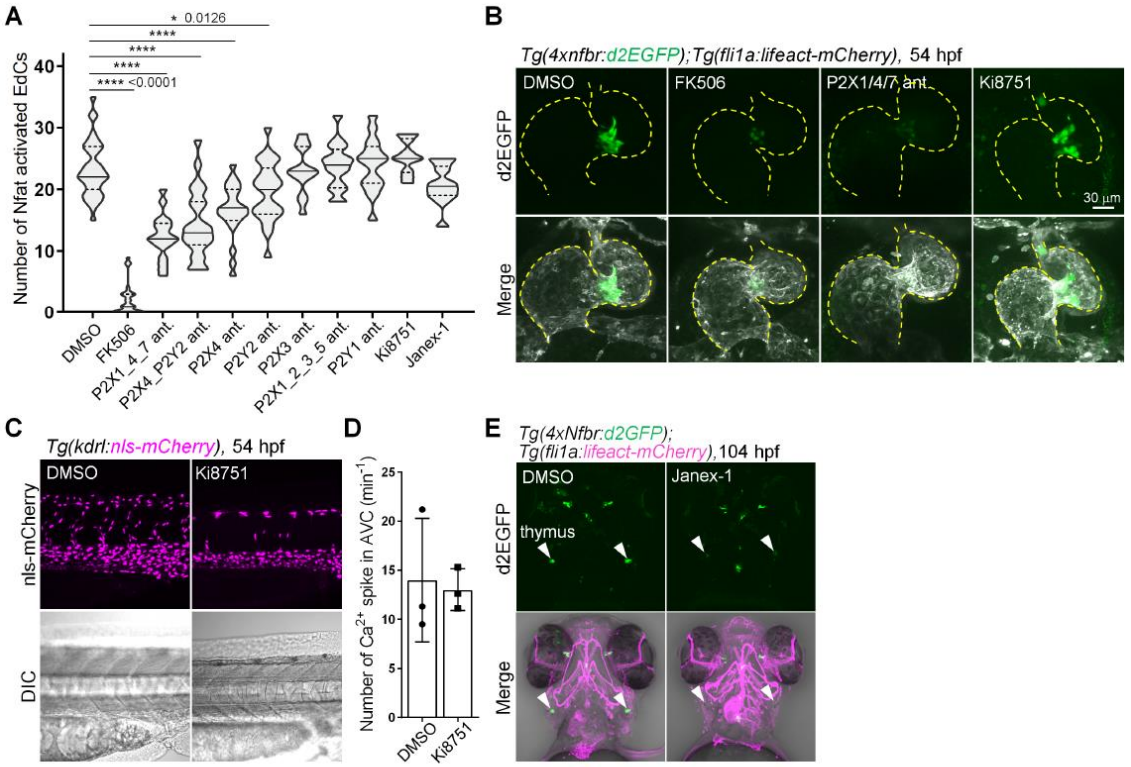

Fukui H et al., Fig. S10

Fig. S9. Several P2Xs/P2Ys coordinately regulate Nfat activity in EdCs. (**A**) Violin plot demonstrating the number of Nfat reporter activated EdCs at 52 hpf in control (DMSO, n = 37), FK506 (n = 12), P2X1_4_7 antagonists (n = 22), P2X4_P2Y2 antagonists (n = 25), P2X4 antagonist (5-BDBD, n = 17), P2Y2 antagonist (AR-C 118925XX, n = 23), P2X3 antagonist (A317491, n = 13), P2X1_2_3_5 antagonist (PPADS tetrasodium salt, n = 16), P2Y1 antagonist (BPT-U, n = 15), VEGFR2 inhibitor (Ki8751, n = 10) and Janex-1 (jak3 inhibitor, n = 12) treatment from 34 hpf to 54 hpf. (**B**) Confocal scanned images of *Tg(4xnfbr:d2EGFP);Tg(fli1a:lifeact-mCherry)* embryonic heart at 54 hpf treated with drugs from 34 hpf to 54 hpf (DMSO, n = 24; FK506, n = 12; P2X1_4_7 antagonists, n = 17; Ki8751, n = 10). Yellow dashed lines indicate the outline of the endocardium. (**C**) Representative images of *Tg(kdrl:nls-mCherry)* embryo at 54 hpf treated with DMSO or Ki8751 from 34 hpf to 54 hpf (DMSO, n = 6; Ki8751, n = 6).

Note that Ki8751 significantly suppresses angiogenesis in the trunk area. Images are taken lateral view, anterior to the left. (**D**) Number of Ca^{2+} spikes in EdCs of the AVC in embryos at 54 hpf treated with DMSO (n = 3) or Ki8751 (n = 3) from 34 hpf to 54 hpf. (**E**) Representative images of *Tg(4xnfbr:d2EGFP);Tg(fli1a:lifeact-mCherry)* embryo at 104 hpf treated with DMSO (n = 10) or Janex-1 (n = 10) from 36 hpf to 104 hpf. Note that Janex-1 significantly suppresses Nfat reporter activity in the thymocyte (arrowheads).

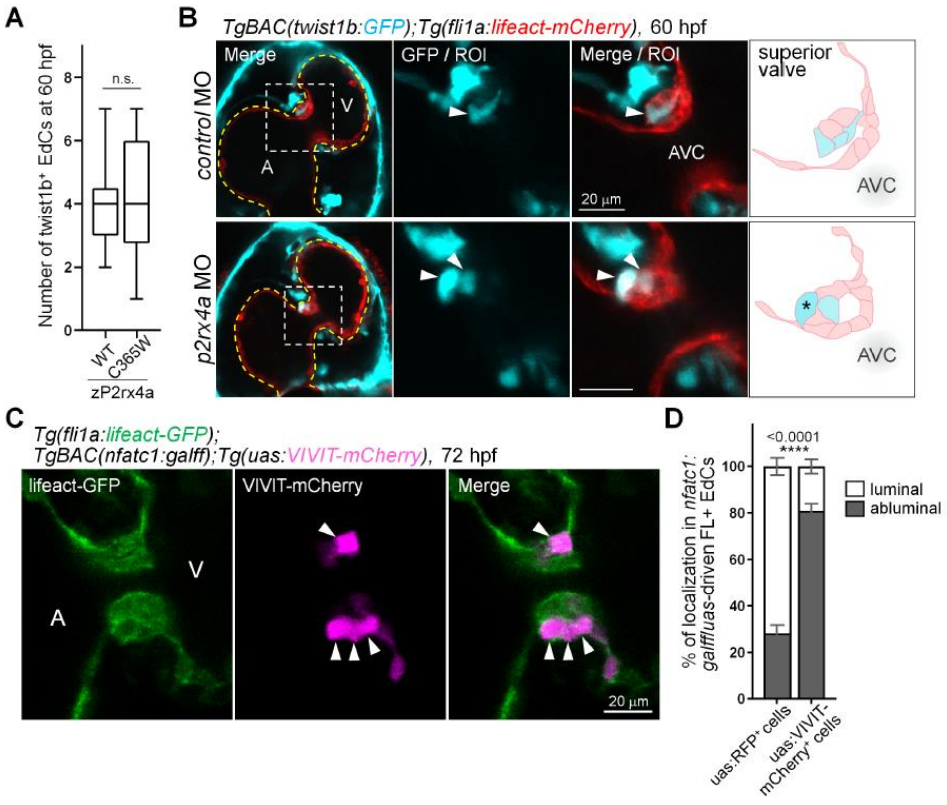

Fukui H et al., Fig. S11

Fig. S10. Nfat-suppressed EdCs are excluded for the luminal area of the AVC. (**A**) Boxplot representing the number of twist1b^{+} EdCs of the AVC in embryos injected with *zp2rx4aWT* (n = 9) and *zp2rx4aC365W* (n = 14) mRNAs at 60 hpf. (**B**) Representative confocal images of *TgBAC(twist1b:GFP);Tg(fli1a:lifeact-mCherry)* embryo injected

582 with *control* MO (n = 6) and *p2rx4a* MO (n = 6) at 60 hpf. Arrowheads indicate the
583 twist1b expression in the EdCs. Yellow dashed lines depict the outline of the endocardium
584 and schematics of the superior valve demonstrate in the right panels. Asterisks indicate
585 the EdCs with an ectopic twist1b expression that protruded from the abnormal region. (**C**)
586 Representative images of *Tg(fli1a:lifeact-GFP);TgBAC(nfatc1:galff);Tg(uas:VIVIT-*
587 *mCherry)* embryo at 72 hpf. Arrowheads indicate the VIVIT-mCherry positive EdCs in
588 the abluminal region of the AVC. (**D**) Quantitative analyses of the luminal / abluminal
589 localisation ratio in the fluorescence positive EdCs under the *TgBAC(nfatc1:galff)* driver
590 crossed with *Tg(uas:RFP)* (left column, n = 19) and with *Tg(uas:VIVIT-mCherry)* (right
591 column, n = 23) at 72 hpf.
592
593
594 **Movie S1.** Single scanned live imaging video (10 msec / frame) of Ca^{2+} influx in EdCs
595 (black, fli1a:galff,uas:GCaMP7a) in a 54 hpf embryo. The video was taken ventral view
596 using lightsheet microscope, anterior to the top. Magenta arrowheads depict the activated
597 GCaMP7a signal in EdCs.
598
599 **Movie S2.** Artificially stopped XYtR heart video (original movie was taken by 20 msec
600 / frame) for ratiometric analysis of Ca^{2+} influx in EdCs (green, fli1a:galff,uas:GCaMP7a)
601 and nuclear-localised mCherry signal in EdCs (magenta, kdrl:Nls-mCherry) at 54 hpf
602 embryo (n = 3). The video was taken ventral view using the spinning disc microscope,
603 anterior to the top. White arrowheads indicate the activated GCaMP7a signal in EdCs.
604
605 **Movie S3.** Single scanned bright field video of the bead grafted embryo at 54 hpf. Ventral

606 view and anterior to the top.

607

608 **Movie S4.** 3D simulation video of wall shear stress in the bead grafted atrial heart region
609 with dynamic wall motion for one cardiac cycle. Shear force intensity was shown by the
610 heat map color.

611

612 **Movie S5.** Single scanned live imaging video (10 msec / frame) of Ca^{2+} influx in EdCs
613 (heat map color, fli1a:galff,uas:GCaMP7a) of the bead grafted embryo at 54 hpf. The
614 bead was retained in the atrium (yellow cycle). Arrowheads depict the activated
615 GCaMP7a signal in EdCs. The video was taken ventral view using a lightsheet
616 microscope, anterior to the top.

617

618 **Movie S6.** Single scanned live imaging video (10 msec / frame) of Ca^{2+} influx in EdCs
619 (heat map color, fli1a:galff,uas:GCaMP7a) of the bead grafted embryo at 54 hpf. The
620 bead was retained in the ventricle (yellow circle). Arrowheads indicate the activated
621 GCaMP7a signal in EdCs. The video was taken ventral view using a lightsheet
622 microscope, anterior to the top.

623

624 **Movie S7.** Single scanned live imaging video (5 sec / frame) of Ca^{2+} influx in EdCs (green,
625 fli1a:galff,uas:GCaMP7a) and nuclear-localised mCherry signal in EdCs (magenta,
626 kdrl:Nls-mCherry) of the magnetic bead grafted embryo at 2 dpf, and the right panel is
627 the DIC image. The magnetic bead (64 μm) was retained in the atrium and the magnetic
628 tweezer was applied after arresting heartbeat. The video was taken left view using an
629 inverted epifluorescent microscope, anterior to the top. White arrowheads depict the

initiation of the activated GCaMP7a signal in EdCs.

Movie S8. Single scanned live imaging video (10 msec / frame) in injection of PBS and fluospheres (black, 0.5 μm) into cardiac lumen of *Tg(fli1a:galff,uas:GCaMP7a)* embryo at 54 hpf. The video was taken ventral view using a lightsheet microscope, anterior to the top. Magenta arrowheads depict the moving fluospheres in response to the blood flow.

Acknowledgements

We thank the member's in J.V.'s lab and in N. Mochizuki's lab for discussion and comments on the manuscript; the entire staff of the imaging facility and the fish facility in IGBMC for their assistance; Y.Y.F. in Y.C.H. lab for tabulation of the simulation results; M.S., A.C. and T.B. in N. Mochizuki's lab for their assistance. **Funding:** J.V. has received funding from the European Research Council (ERC) under the European Union's Horizon 2020 research and innovation program: H.F. was supported from the University of Strasbourg Institute for Advanced Study (USIAS-2017-097), Takeda Medical Research Foundation, Uehara Memorial Foundation, and Cell Science Research Foundation. **Author contributions:** H.F. and J.V. conceived the project. H.F. designed the work and performed experiments. R.W.C. performed the analysis of Ca^{2+} signaling normalization. H.F., J.X. and N. Minc performed the magnetic tweezer experiments. V.V. and Y.C.H. performed the analysis of 3D simulation. N. Minc and N. Mochizuki provided reagents and suggestions. H.F. and J.V. wrote the manuscript. All authors interpreted the data, contributed to data analysis and discussed the manuscript. **Competing interests:** The authors declare no competing interests. **Data and materials availability:** All images

and Tg lines are available in the main text or the supporting materials.

Corresponding authors

Materials and Methods:

Zebrafish (*Danio rerio*) strains, transgenic lines, and mutant lines

The experiments using zebrafish were approved by the animal experimentation committee of the institutional review board of the IGBMC (reference numbers MIN APAFIS#4669–2016032411093030 v4 and MIN 4669–2016032411093030 v4-detail of entry 1) and performed according to the guidelines of the Institute. Embryos were raised in E3 medium and incubated at 28.5°C. Developmental staging was referred to chronological and morphological criteria (*68*). We used the AB strain as wild-type. The following zebrafish transgenic lines were used for experiments: *Tg(fli1a:gal4ff)* (*69*), *Tg(uas:GCaMP7a)* (*70*), *Tg(kdrl:nls-mCherry)*^{ncv5} (*71*), *Tg(fli1a:lifeact-mCherry)*^{ncv7} (*72*), *Tg(tp1:d2EGFP)* (*73*), *Tg(fli1a:myr-mCherry)*^{ncv1} (*74*), *Tg(fli1a:h2b-mCherry)*^{ncv31} (24), *Tg(myl7:nls-mCherry)*^{ncv11} (*75*), *Tg(uas:RFP)* (*76*), and *TgBAC(nfatc1:gal4ff)* (*65*). The *Tg(4xnfbr:d2EGFP)*^{ncv531}, *TgBAC(twist1b:GFP)*^{ncv534}, *Tg(fli1a:GFP-nfatc1)*^{ncv532}, and *Tg(uas:VIVIT-mCherry)*^{ncv533} were generated as described in the experimental procedures. We used FK506, a calcineurin inhibitor, which is blocking valve morphogenesis to test the specificity in the *Tg(fli1a:lifeact-GFP);Tg(kdrl:nls-mCherry)* embryos (*25*, *40*) (Fig. S2D). Such treatment significantly suppressed the reporter expression of *Tg(4xnfbr:d2EGFP)* embryos (Fig. S10, A and B). In addition, VIVIT peptide overexpression using a selective inhibitor of Nfat dephosphorylation (*77*), using the *TgBAC(nfatc1:galff)* driver which is specific to endocardial cells (*65*) was used.

Such treatment also led to the suppression of reporter activation (Fig. S2E), demonstrating that our reporter *Tg(4xnfbr:d2EGFP)* is indeed revealing Nfat activation. The following zebrafish mutants were used for experiments: The knockout alleles of *m651* for *gata1a (33)*, *ts294e* for *dzip1 (53)*, *tc321* for *trpp2 (52)*, *sa1671* for *trpv4* (*4*) (Zebrafish International Resource Center [ZIRC]), *sa12608* for *piezo1* (European Zebrafish Resource Center [EZRC]), *sa12414* for *piezo2a* (ZIRC), *sa14724* for *piezo2b* (ZIRC). The knockout allele of *ncvxx* for *p2rx1* and ncvxx for *p2rx4a* were generated as described in the experimental procedures.

Generation of knockout zebrafish by TALEN mutagenesis

To develop knockout zebrafish, we used transcription activator-like effector nuclease (TALEN) Targeter 2.0 (https://tale-nt.cac.cornell.edu) to design TALEN pair that targets *p2rx1* and *p2rx4a*. The target sequence of TAL-*p2rx1 and* TAL-*p2rx4a* were 5'-TGCCATCGGCTCAGTCTTCACcaagatgaagggagtgTCCTTCACTAATATCAGTGGA-3', and 5'-TTCTCAGCTCAGTCACaaccaaagtgaaaggAATTGCTTTAACAAACACCA-3', respectively (capital letters were sequences of left [TAL-*p2rx1*-F and TAL-*p2rx4a*-F] and right [TAL-*p2rx1*-R and *p2rx4a*-R] arms, respectively). These expression plasmids of the TALEN-pair were constructed by pT3TS-GoldyTALEN. TALEN mRNAs were synthesized *in vitro* by T3 mMessage mMACHINE kit (Thermo Fisher Scientific). To induce double strand breaks in the target sequence, both 50 pg of TAL-*p2rx1-F* / *-p2rx1-R* mRNAs, and TAL-*p2rx4a-F* / *-p2rx4a-R* mRNAs were injected into 1-2-cell stage transgenic embryos, respectively. Each injected founder (F0) fish was outcrossed to wild-type fish to obtain the F1 progeny from individual founders. To analyse TALEN induced mutations, genomic DNA from F1 embryos was lysed by 50 µl

of NaOH solution (50 mM) at 95°C for 5 min, and 5 μl of Tris-HCl (pH8.0, 1.0 M) was added on ice for 10 min. After centrifugation (13,500 rpm, 5 min), PCR reaction was performed by KOD FX Neo DNA polymerase (TOYOBO). The genotyping PCR primers were used for amplification: *p2rx1* (5'-GTGTGGAGCCCTGCAATTTTTAC-3' and 5'-CAACCCACCTGTTCAGGAAACAC-3', 60°C for annealing); *p2rx4a* (5'-TCATAGCCTACGTTATCGGGTAAG-3' and 5'-CACCAGTGAGTGGTCTGGTCATT-3', 60°C for annealing).

Genotyping primers

The following genotyping PCR primers were used for amplification: *piezo1* (5'-CTATTCCTTTGAGAGCCCTTTG-3' and 5'-GCATGTGGATACAGCAATGAC-3', 58°C for annealing); *piezo2a* (5'-AATGTGATGTGTTGCTCTGC-3' and 5'-CTTTCAGCAAAGGCATCTCC-3', 60°C for annealing, and for sequence; 5'-TCAGTCTGTTCGGGATTTCTC-3'); *piezo2b* (5'-TGCTAGGTGGTTGGCTTTCTC-3' and 5'-CTTAAAGCTGTGAAGGAGACATC-3', 65°C for annealing, and for sequence; 5'-TCTCTGTGGAACTGATGTTGTG-3'); *gata1a* (5'-GTGAGTATACACAATTACAC-3' and 5'-GGTTCAGAGAATACGCTCCT-3', 53°C for annealing); *trpv4* (5'-GCCTTTCAGCATGTTGTCCA-3' and 5'-GGTTCCTGCTGGTCTACGTG-3', 56°C for annealing); *trpp2* (5'-CCATTAGCCTGCACATTCAATC-3' and 5'-ATCGCACTGCTCATCTGAAG-3', 68°C for annealing); *dzip1* (5'-CGGTACAGACACAGCCCAATG-3' and 5'-CGTGAGACCAGTGTAGGTTC-3', 60°C for annealing, and for sequence; 5'-ACAAACAAATTCAAGTCCAG-3').

Image acquisition and definition of the AVC

To clearly obtain images of embryos, a 0.2 mM solution of 1-phenyl-2-thiourea (PTU) (Sigma-Aldrich) was added in breeding E3 media to suppress pigmentation and 0.1 mg/mL of MS-222 was added to anesthetize the embryos during embedding. A TCS SP8 DLS light sheet confocal microscope (Leica) equipped with 25x water immersion objective (Leica HCX IRAPO L, 0.95 N.A.) and a camera (ORCA-Flash4.0 V2, Hamamatsu) for acquisition. A Lightsheet Z.1 (Zeiss) equipped with 20x water immersion objective (Zeiss, 1.0 N.A.) and two cameras (PCO.edge sCMOS) for simultaneous acquisition. An inverted microscope (Leica, DMi8) combined with a CSU-X1 confocal scanning head (Yokogawa) equipped with a 40x water objective (Leica, 1.1 N.A.) and two cameras (ORCA-Flash4.0 V2, Hamamatsu) for simultaneous acquisition. Ca^{2+} influx was visualized by the excitation of the genetically encoded calcium indicator GCaMP7a using a 488 nm wavelength laser line. Excitation of GFP and mCherry was done using 488 nm and 561 nm wavelength laser lines, respectively. Beating heart samples were taken every 10 msec exposure time unless otherwise described and the data were acquired by binning 2 x 2. Confocal images of 1.5 μm steps were taken with an upright TCS SP8 confocal microscope system (Leica) equipped with a 25x water immersion objective (Leica HCX IRAPO L, 0.95 N.A.) and an upright FV3000 confocal microscope system (Olympus) equipped with a 20x water immersion objective (Olympus XLUMPlan FL_N, 1.0 N.A.). Dechorionated embryos were mounted in 1% low-melting agarose (Invitrogen-Thermo Fisher Scientific) dissolved in E3 medium. At early stages (30 hpf and 34 hpf), the pre-AVC region is defined as the middle area between arterial pole and venous pole. Furthermore, the tissue curvature is found in the pre-AVC region and used as morphological landmarks. After 48 hpf, the endocardial cells on the AVC

region is defined by the area located between the superior and inferior region of the atrium and the ventricular chamber. Images were processed with a Las X software (Leica), Zen 3.1 software (Zeiss), FV31S-SW software (Olympus), ImageJ and Imaris 9.6 (Bitplane).

Chemical treatments

Embryos were treated with the following small molecule inhibitors: MS-222 (2.0 mg/mL) or BDM (2,3-butanedione monoxime, 30 mM, Sigma-Aldrich) to induce heart arrest; p-amino-blebbistatin (10 μM, Optopharma), a myosin II inhibitor, to suppress a heartbeat without block the action potential; Gadolinium chloride ($GdCl_3$, 0.2 mM and 1 mM, Sigma-Aldrich), a stretch-activated calcium channel inhibitor, to check the influence of Ca^{2+} influx in EdCs of the AVC; Oligomycin A (50 μg/mL, Sigma-Aldrich), an inhibitor of mitochondrial ATP synthetase, to reduce the ATP level; 5-BDBD (10 μM, Sigma-Aldrich), a P2X4 antagonist, to check the function of P2rx4 in the EdCs; NF023 (10 μM, Tocris), a P2X1 antagonist, to check the function of P2rx1 in the EdCs; A-317491 (10 μM, Sigma-Aldrich), a P2X3 antagonist, to check the function of P2rx3 in the EdCs; A-438079 (10 μM, Sigma-Aldrich), a P2X7 antagonist, to check the function of P2rx7 in the EdCs; PPADS tetrasodium salt (20 μM, Tocris), a P2X1, X2, X3 and X5 non-selective antagonist, to check the function of P2X1_2_3_5 in the EdCs; BPTU (25 μM, Tocris), a P2Y1 antagonist, to check the function of P2Y1 in the EdCs; AR-C118925XX (10 μM, Tocris), a P2Y2 antagonist, to check the function of P2Y2 in the EdCs; FK506 (2 μM, Abcam), a calcineurin inhibitor, to validate Nfat reporter activity; Janex-1 (0.4 mM, Abcam), a Jak3 inhibitor, to validate Nfat tyrosine phosphorylation (*78*); Ki8751 (1 μM, Tocris), a VEGFR2 inhibitor, to check the effect of Vegfr2 signaling in the EdCs. As a control, the embryos were incubated in E3 solution containing DMSO.

774

775 **Microsurgery to retain the bead into cardiac lumen**

776 Zebrafish embryos were kept ventral side to the top and embedded with 1% low-melting
777 agarose. After mounted, beads (PureCube Glutathione MagBeads, Cube Biotech) were
778 deposited on top of the agarose with E3 medium. A hole was created in the center of the
779 yolk by forceps and the bead of roughly 30-40 μm diameter was inserted into a hole. The
780 bead was pushed anteriorly by the tip of forceps. Once the bead reached the venous pole,
781 suction caused by the heart contraction will move the bead into the cardiac lumen (*79*).
782 Embryos then were released from agarose and allowed to develop in E3 medium at 28.5^{o}C.
783 Approximately 30% embryos kept the bead move continuously in the atrium or the
784 ventricle together with the blood flow were applied to the experiments. Whereas, the
785 embryos with the bead sucked in the outflow tract were excluded for the experiments.

786

787 **Simulation of influences in the grafted bead in the atrium**

788 A static geometry of the zebrafish atrium was approximated from a 2D fluorescent
789 imaging video of the atrial chamber containing the moving magnetic bead. 2D outlines
790 of the atrial wall and AVC were extracted from the video, imported in ANSYS
791 Workbench 2019 (ANSYS Inc.) and revolved about their respective central axes to
792 generate a 3D shape of the atrial chamber and AVC (Fig. S3A). A 30 μm spherical bead
793 was inserted in the chamber. The atrial chamber was meshed with about 453k tetrahedral
794 cells, and a zone of 30 μm radius from the center of the bead was programmed to have an
795 overset mesh with 384k tetrahedral cells, which were determined by a mesh convergence
796 study. In both meshes, refined mesh at wall boundaries was achieved via 5-10 inflation
797 layers. The overset mesh was superimposed onto the atrial chamber mesh, and together

with the bead, was programmed to move with a uni-directional oscillatory motion via ANSYS user-defined function. The bead motion waveform (Fig. S3B) was traced from the 2D video mentioned above. The bead motion was stopped at about 0.44 μm from the atrial wall to avoid numerical problems as an estimation of the impingement. The blood fluid in the atrial chamber was assumed to have a viscosity of 3.5 cP and density of 1060 kg/m^3. The inlet and outlet boundary conditions were set to zero reference pressures. Two cardiac cycle (800 time-steps) was simulated, with results were extracted from the second cycle. In another variant of the simulation, flow velocities were estimated from the inlet boundary via blood cell motions in the video and were imposed as inlet flow boundary conditions to give a more realistic boundary condition, but the results did not vary significant, and this was thus not considered. The limitation of the simulation was that there were no consideration of the motion of the atrial walls, however, given that the bead motion velocity was higher order than atrial wall motion velocity, our simulations' estimate of the peak wall shear stress and pressures at the bead impact location on the atrial wall should still be reasonable reliable.

Magnetic tweezer

A magnetic tweezer was used to apply force to magnetic beads (PureCube Glutathione MagBeads, Cube Biotech) (*80*, *81*) grafted into embryos. Embryos were kept on their lateral side and embedded into 1% low-melting agarose and the heartbeat was arrested by addition of BDM or tricaine into E3 medium. The magnetic probe was built from three rod-shaped, strong neodymium magnets (diameter, 4 mm; height, 10 mm; S-04-10-AN; Supermagnet) prolonged by a sharpened steel piece with a tip radius of ~50 μm to create a magnetic gradient. The surface of the steel tip was electro-coated with gold to prevent

oxidization. The magnetic tweezers were mounted on an inverted epifluorescent microscope (TI-Eclipse, Nikon) combined with a CMOS camera (Hamamatsu), and its position was controlled by a micromanipulator (Injectman 4, Eppendorf). Embryos were filmed with a 20x dry objective (Apo, NA 0.75, Nikon) and a 1.5x magnifier. The microscope was operated with Micro-Manager (Open Imaging). The embryos with the injected beads in the heart were rotated to become aligned with the principal axis of the magnetic tweezer and time-lapse movies were acquired with a time interval of 5 sec. In each experiment, the magnetic force was controlled by the magnet position to shear and/or compress the cells. The positions of the magnet tip and the agarose magbead were recorded in DIC, and the endocardial cells and Ca^{2+} signaling were recorded in fluorescence.

The magnetic force was calibrated by first charactering the large-scale magnetic force field created by the magnet tip. For this, 2.8 μm mono-dispersed magnetic beads were pulled in a viscous test fluid (80% glycerol, viscosity $8.0*10^{-2}$ Pa*sec at 22°C) by the magnet to track the beads velocity as a function of the distance to the magnet, yielding:

$$V = 195.4 * e^{-\frac{x}{31.3}} + 31.94 * e^{-\frac{x}{84.05}}$$

$$V_{300} = 0.9134\ \mu m/s$$

where V is the velocity of the magnetic bead and x is the distance between the bead and the magnet tip. V_{300} is the bead velocity at a distance 300 μm away from the magnet tip.

The same experiment performed on agarose magnetic beads with varying sizes at a fixed distance of 300 μm then allowed to compute the net magnetic force, and establish force-size relationships, using the Stokes equation.

$$F_{300} = 0.1533 * R^3$$

where R is the bead radium (μm). F_{300} is the magnetic force (pN) at a fix distance 300 μm from the magnet tip.

According to velocity-distance and force-size relationships, we computed the final equation for calculating the magnetic force:

$$F = 0.1533 * R^3 * \frac{V_x}{V_{300}}$$

where F is the magnetic force (pN), and V_x (μm/s) is the velocity at x μm in the magnetic field. Pressure and shear stresses were deduced by projecting the forces, orthogonal or parallel to the tissue plane, respectively, and by dividing them a measured contact surface area between the bead and the tissue.

Microinjection into cardiac lumen

Tg(fli1a:galff);Tg(uas:GCaMP7a);Tg(kdrl:nls-mCherry) embryos were kept lateral side and embedded into 1% low-melting agarose. After mounted, we injected with 2 nL of apyrase (0.9 U/μL, Sigma-Aldrich), ATPγS tetralithium salt (45 mM, Tocris), and Oligomycin A (25 μg/mL) together with red fluorescent 0.5 μm Fluospheres (Thermo Fisher Scientific) using Nanoject II (Drummond) into the region of common cardinal vein. To confirm the precise injection, circulation of Fluospheres in cardiac lumen was checked by the fluorescent stereo zoom microscope (Leica MZ FLIII), and a lightsheet microscope was used to evaluate the Ca^{2+} influx.

Microinjection of MOs, mRNAs and Tol2 plasmids

We injected 1 nL of the following Morpholino oligonucleotides (MOs, Gene Tools): 0.5 mM of *gata1a* atg-MO (5'-CTGCAAGTGTAGTATTGAAGATGTC-3') (*34*); 0.15 mM of *tnnt2a* atg-MO (5'-CATGTTTGCTCTGATCTGACACGCA-3') (*82*); 0.6 mM of *control* MO (5'-CCTCTTACCTCAGTTACAATTTATA-3'); 0.6 mM of *trpp2* atg-MO (5'-AGGACGAACGCGACTGGAGCTCATC-3') (*83*); 0.6 mM of *kif3a* atg-MO (5'-GTCCAGCTTATTGCTCGGCATTATC-3') (*84*); 0.35 mM of *myh6* atg-MO (5'-ACTCTGCCATTAAAGCATCACCCAT-3') (*85*); 0.3 mM of *p2rx4a* splice-MO (5'-AAATGCTGAGCCATACCATCTCCAC-3'). To check the *p2rx4a* MO efficiency, we used following primers; 5'-TCGTGCTGACCAACATGATCATCAC-3' and 5'-TTCGGGGGATCGACAATTTTTTCT-3'. MOs, mRNAs, and Tol2 plasmids were injected into blastomeres using Nanoject II (Drummond) and IM300 Microinjector (Narishige) at one- to two-cell stage.

Plasmids

cDNA fragments encoding zebrafish Klf2a, Klf4a, Egr1, Notch1b, P2rx1, P2rx4a and P2rx7 were amplified by PCR using Phusion high-fidelity PCR master mix (Thermo Fisher Scientific) and a cDNAs library derived from zebrafish embryos, and subcloned into pCR4 Blunt TOPO vector (Thermo Fisher Scientific). The following primers set were used for amplification: *klf2a* (5'-aactcgagAAGGATGAACTGGACAGGTCCATG-3' [containing XhoI sequence] and 5'-CTGTGATGAGCCTTCAAGTGAGAAC-3'); *klf4a* (5'-aactcgagGAGCTGGAGCTGCTGGACTATGACT-3' [containing XhoI sequence] and 5'-CGCTGTCAGCGTTGGTATTATATC-3'); *egr1* (5'-

889 aactcgagAGCAGTTTGATCACCTTGCTGGAG-3’ [containing XhoI sequence] and 5’-
890 TTCTGTCCTGTGTGGATGCGGATG-3’); *p2rx1* (5’-
891 aagctagcGGTGTTCATGTATGAGAAAGGCTACC-3’ [containing NheI sequence] and
892 5’-CGCTGTCAGCGTTGGTATTATATC-3’); *p2rx4a* (5’-
893 aagctagcGTGTGTCTACAACAAAGGCTACCAAG-3’ [containing NheI sequence] and
894 5’-CAATCCAGTCACAGATGACGTTCAC-3’); *p2rx7* (5’-
895 aagctagcACCTGCTCTTTTGGCTGCAGCAGAAA-3’ [containing NheI sequence] and
896 5’- GACGAAGACTGTATGGTCTCCAGTA-3’).
897 The cDNA of humanP2X4 and zebrafishP2rX4a are cloned into pmCherry-N1 vector and
898 mutated C353W and C365W, respectively. The following primers were used for cloning:
899 NheI-hP2X4WT-S (5’-aaGCTAGCccATGgcgggctgctgcgccgc-3’) and AgeI-hP2X4WT-
900 AS (5’-atACCGGTtgctggtccagctcactagcaaga-3’); hP2X4C353W-S (5’-
901 gtgctgTGGgacatcatagtcctctac-3’) and hP2X4C353W-AS (5’-
902 gatgtcCCAcagcacggtcgccatgcc-3’); NheI-zP2rx4aWT-S (5’-
903 caGCTAGCgttcacaATGagtgaaagtgttgg-3’) and AgeI-zP2rx4aWT-AS (5’-
904 atACCGGTtgtttgtcttcgttgtgtaaaagtccg-3’); zP2rx4aC365W-S (5’-
905 gtcatcTGGgactggattgtgttgaca-3’) and zP2rx4aC365W-AS (5’-
906 ccagtcCCAgatgacgttcaccaggcct-3’). These cDNAs (hP2X4WT, hP2X4C353W,
907 zP2rx4aWT and zP2rx4aC365W) were subcloned into the pCS2 vector (Clontech) and
908 synthesized capped mRNAs using mMESSAGE mMACHINE T7 transcription kit
909 (Thermo Fisher Scientific). The embryos were injected 125 pg of each mRNAs into
910 blastomeres at one- to two-cell stage. All these cDNAs and mutations were confirmed by
911 DNA sequencing.
912

Generation of transgenic lines

To monitor the nfat signal activation, we established a transgenic reporter zebrafish line expressing destabilized EGFP (d2EGFP) under the control of four times Nfat binding element tandem sequence repeats (4xnfbr)-dependent E1b minimal promoter activation; *Tg(4xnfbr:d2EGFP)*^{ncv531}. The primers based on 1xNfbr sequence (*77*) attached with flanking XhoI (G/TCGAC) and SalI (C/TCGAG) site (XhoI-1xNfbr-SalI-S, 5'-TCGAGacgccttctgtatgaaacagtttttccaggG-3'; XhoI-1xNfbr-SalI-AS, 5'-TCGACcctggaaaaactgtttcatacagaaggcgtC-3'; small letters represent 1x nfat binding element) were ligated together to make a single linear DNA fragment and digested the products with XhoI and SalI to eliminate the inverted repeats as these DNAs contain reconstituted XhoI and SalI sites. DNA fragments were applied agarose gel electrophoresis and collected a fragment around the 150 bp as a 4x tandem oligomers. A 4xnfbr tandem oligomers were ligated into both XhoI and SalI-digested pTol2 fragment to make a pTol2-4xnfbr vector. The sequence of 4x tandem repeats was confirmed by DNA sequence. pTol2-4xnfbr vector was inserted with E1b minimal promoter and d2EGFP-polyA sequence to construct the pTol2-4xNfbr-E1b-d2EGFP-pA plasmid.

To monitor the nfat signal inhibition, we established a transgenic line expressing VIVIT-mCherry under the control of Gal4-UAS system; *Tg(uas:VIVIT-mCherry)*^{ncv533}. We used a pmCherry-N1 vector as a template and VIVIT peptide (MAGPHPVIVITGPHEE) oligo sequence is inserted upstream of mCherry site by inverse PCR using the following primers: VIVIT-mCherry-S; 5'-atggcgggaccacacccagtaatcgtaattaccggtccacacgaggaggggccccctgtcgctagcATGGTGAGC AAGGGCGAGGAGGATAAC-3' and VIVIT-mCherry-AS; 5'-GGTGGCGACCGGTGGATCCCGGGCCCGCGGTAC-3' to make VIVIT-mCherry-

pA plasmid. The fragment of VIVIT-mCherry-pA site is inserted into pTol2-crystallin-Nls-mCherry-5xuas vector to establish the pTol2-crystallin-Nls-mCherry-5xuas-VIVIT-mCherry-pA plasmid.

To monitor the EndoMT, we established a GFP reporter transgenic line under the control of *twist1b* BAC enhancer/promoter; *TgBAC(twist1b:GFP)*^{ncv534}. pRedET plasmid (Gene Bridges, Heidelberg, Germany) was introduced into E. coli containing CH73-181M7 BAC clone encoding *twist1b* gene (BacPAC resources) by electroporation (1800V, 25 mF, 200 Ω). Tol2 long terminal repeats in opposite directions flanking ampicillin resistance cassette were amplified by PCR using Tol2_amp as a template and were inserted into the BAC vector backbone. The cDNA encoding GFP together with a kanamycin resistance cassette (GFP_KanR) was amplified by PCR using pCS2-GFP_KanR plasmid as a template and inserted into the start ATG of the *twist1b* gene. Primers to amplify the GFP_KanR for *twist1b* were 5'-atgctggaataacgtccttattcgcacgcgctttcagcagagacttaagcACCATGGTGAGCAAGGGCGAG GAG-3' and 5'-tccgcgggagacacgggggagctggaggagtctcgcgcgggctcttcgggTCAGAAGAACTCGTCAAG AAGGCG-3' (small letters; homology arm to BAC vector, and capital letters; primer binding site to the template plasmid).

To monitor the subcellular localization of Nfatc1 in the EdCs, we established a transgenic line expressing GFP-tagged Nfatc1 under the control of *fli1a* promoter; *Tg(fli1a:GFP-Nfatc1)*^{ncv532}. Primers to amplify the human-Nfatc1 (hNfatc1) were (5'-agatctCCAAGCACCAGCTTTCCAGTCCCTTC-3' [containing BglII sequence] and 5'-gtcgacCAGTTAAATGTGCAACACGCCAC-3' [containing SalI sequence]). The construct was inserted into the pEGFP-C1 vector to establish pEGFP-hNfatc1. The

EGFP-hNfatc1 was inserted into pTol2-fli1epEGFP-DEST (Addgene #73491) backbone vector to establish the pTol2-fli1a promoter-GFP-Nfatc1.

Tol2-mediated zebrafish transgenesis was performed by injecting 30 pg of transgene plasmid together with 50 pg of *tol2 transposase* mRNA, followed by subsequent screening of F1 founders and establishment of stable transgenic strains through selection in F3 generations.

Ca^{2+} influx normalisation

To monitor the Ca^{2+} signal during heart development, we crossed the *Tg(fli1a:gal4ff);Tg(uas:GCaMP7a)* line, where a fluorescent Ca^{2+} sensor protein GCaMP7a is driven by endocardial gal4, with the *Tg(kdrl:nls-mCherry)* line, where kdrl-promoter drives nls-mCherry and thus labels endocardial nuclei. To measure the normalised calcium signal of a particular cell over time, we developed software in Matlab (Mathworks) to do the following: For each embryo, the cells imaged move in and out of the focus plane during heartbeat, causing fluctuations in the detectable calcium signal. Our first step was thus to transform our XYT movies into XYtR movies, where T is the timepoints acquired, t is the timepoint along the cardiac cycle, and R is the iteration of cardiac cycles. To do so, we must account for the changes in heartrate over the period of imaging. Using Matlab, we selected nine region of interests (ROIs) one tenth of the size of the whole image and measured the fluorescence intensity of the nuclear channel over time, $I_{nuclear}(T)$. We calculate the position of the intensity peaks based using ct_getpeaks (*86*) and select two ROIs where the fluctuations in nuclear channel intensity due to heartbeat are the clearest. Next, we averaged the peak positions acquired from the two ROIs iteratively. Each of these averaged peak positions are assumed to correlate to a

specific position within the cardiac cycle. We then calculated the average number of timepoints between these peaks to get the average period of heartbeat t_{max}. We cut the XYT movie into sections with length of (t_{max} + 7 images); each centered around the image corresponding to the averaged peak position. We then recombined the sections into a XYtR movie.

For each cell of interest within the embryo, we created XYR movie: The XYtR movie is opened in FIJI, the timepoint along the cardiac cycle that best captures the cell of interest was manually identified, and an XYR movie was created for that timepoint. *Image of average signal*: Importing the XYR movie back into Matlab, an image that showed the average calcium and average nuclear signal over the entire course of imaging was calculated. For both channels, each pixel in the final image is the sum of the signal intensity divided over the total number of images, R_{max}. *Normalised calcium signal*: Using the image of the average signal as a guide, we manually drew around the cell of interest to generate the ROI. The normalised calcium signal for the ROI was then calculated using: where $I_{calcium}$ is the fluorescence intensity of the calcium signal, $I_{nuclear}$ is the fluorescence intensity of the nuclear signal, and the baseline is the minimum $I_{calcium}/I_{nuclear}$ over the entire XYR movie. *Calculate peak position*: The position of the peaks was calculated using ct_pulseanalysis (*86*) with the SMOOTH parameter set to 5.

Whole-mount in situ hybridization (WISH)

The antisense *klf2a*, *klf4a*, *egr1*, *p2rx1*, *p2rx4a and p2rx7* RNA probes labeled with digoxigenin (DIG) were prepared by using an RNA labeling kit (Roche). WISH was performed as previously described (*87*). Colorimetric reaction was carried out using BM purple (Roche) as the substrate. To stop the reaction, embryos were washed with PBS-T,

fixed with 4% PFA for 20 min at room temperature and subsequently immersed in glycerol. Images were taken using a stereo microscope (Leica M165C).

RNAscope analysis

Embryos were fixed by 10% NBF for overnight at room temperature. After fixation, the solution was changed to 50% Methanol / PBBT (PBS with 2 mg/mL BSA and 0.1% TritonX-100) for 10 min, then changed to 100% Methanol at room temperature, and then stored in 100% Methanol at -20^{o}C overnight. After rehydration, embryos were washed three-times for 10 min in PBBT. Embryos were treated in PBBT with protease plus for 30 min at room temperature, and subsequently washed three-times for 10 min in PBBT. For the probe hybridization, embryos were treated in the following probe mixture (ACDbio): *kdrl*-C1 probe with *p2rx1*-C3, *p2rx4a*-C3 or *p2rx7*-C3 probes; *klf4a*-C1 probe with *klf2a*-C2 probe; *wnt9b*-C1 probe with *klf2a*-C2 probe; *kdrl*-C1 probe with *gata1a*-C3 probe for overnight at 40^{o}C. Embryos were washed and amplified the hybridization following the workflow in ACDbio. Embryos were and stored in PBBT at 4^{o}C prior to confocal imaging.

Data analysis

Data was analyzed using GraphPad Prism 7 (GraphPad Software). All columns are indicated as mean ± s.d. Statistical significance of multiple groups was determined by one-way ANOVA with Tukey's tests. Statistical significance among two groups was determined by Student's t-test with a two-tailed distribution. Data were considered statistically significant if the p-value <0.05 (*), <0.01 (**), <0.0001 (****).

Reference List

1. T. Iskratsch, H. Wolfenson, M. P. Sheetz, *Nat. Rev. Mol. Cell Biol.* **15**, 825-833 (2014).
2. T. Mammoto, A. Mammoto, D. E. Ingber, *Annu. Rev. Cell Dev. Biol.* **29**, 27-61 (2013).
3. D. J. Beech, A. C. Kalli, *Arterioscler. Thromb. Vasc. Biol.* **39**, 2228-2239 (2019).
4. E. Heckel *et al.*, *Curr. Biol.* **25**, 1354-1361 (2015).
5. S. S. Ranade *et al.*, *Proc. Natl. Acad. Sci. U. S. A* **111**, 10347-10352 (2014).
6. J. Xu *et al.*, *Cell* **173**, 762-775 (2018).
7. J. I. Hoffman, S. Kaplan, *J. Am. Coll. Cardiol.* **39**, 1890-1900 (2002).
8. C. Dina *et al.*, *Nat. Genet.* **47**, 1206-1211 (2015).
9. R. Durst *et al.*, *Nature* **525**, 109-113 (2015).
10. V. Garg *et al.*, *Nature* **437**, 270-274 (2005).
11. A. A. Richards, V. Garg, *Curr. Cardiol. Rev.* **6**, 91-97 (2010).
12. M. P. White *et al.*, *J. Mol. Cell Cardiol.* **84**, 13-23 (2015).
13. R. A. Levine *et al.*, *Nat. Rev. Cardiol.* **12**, 689-710 (2015).
14. N. Baeyens, C. Bandyopadhyay, B. G. Coon, S. Yun, M. A. Schwartz, *J. Clin. Invest* **126**, 821-828 (2016).
15. M. A. Schwartz, D. Vestweber, M. Simons, *Science* **360**, 270-271 (2018).
16. K. Yamamoto *et al.*, *J. Cell Sci.* **124**, 3477-3483 (2011).
17. R. M. Davidson, D. W. Tatakis, A. L. Auerbach, *Pflugers Arch.* **416**, 646-651 (1990).
18. J. B. Lansman, T. J. Hallam, T. J. Rink, *Nature* **325**, 811-813 (1987).

19. C. Wei *et al.*, *Nature* **457**, 901-905 (2009).

20. S. Xu, A. D. Chisholm, *Curr. Biol.* **21**, 1960-1967 (2011).

21. W. S. Beane, J. Morokuma, D. S. Adams, M. Levin, *Chem. Biol.* **18**, 77-89 (2011).

22. M. Levin, C. G. Stevenson, *Annu. Rev. Biomed. Eng* **14**, 295-323 (2012).

23. J. G. Goetz *et al.*, *Cell Rep.* **6**, 799-808 (2014).

24. Y. Yokota *et al.*, *Elife.* **4**, (2015).

25. C. P. Chang *et al.*, *Cell* **118**, 649-663 (2004).

26. F. Gunawan, A. Gentile, S. Gauvrit, D. Stainier, A. Bensimon-Brito, *Circ. Res.* (2020).

27. A. M. Ranger *et al.*, *Nature* **392**, 186-190 (1998).

28. B. Zhou *et al.*, *Development* **132**, 1137-1146 (2005).

29. R. A. Schulz, K. E. Yutzey, *Dev. Biol.* **266**, 1-16 (2004).

30. B. Wu, H. S. Baldwin, B. Zhou, *Trends Cardiovasc. Med.* **23**, 294-300 (2013).

31. W. M. Flanagan, B. Corthesy, R. J. Bram, G. R. Crabtree, *Nature* **352**, 803-807 (1991).

32. J. L. Galloway, R. A. Wingert, C. Thisse, B. Thisse, L. I. Zon, *Dev. Cell* **8**, 109-116 (2005).

33. S. E. Lyons *et al.*, *Proc. Natl. Acad. Sci. U. S. A* **99**, 5454-5459 (2002).

34. J. Vermot *et al.*, *PLoS. Biol.* **7**, e1000246 (2009).

35. F. Boselli, E. Steed, J. B. Freund, J. Vermot, *Development* **144**, 4322-4327 (2017).

36. J. B. Freund, J. Vermot, *Biophys. J.* **106**, 752-762 (2014).

37. T. Bartman *et al.*, *PLoS. Biol.* **2**, E129 (2004).

38. Y. Y. Foo *et al.*, *Biomech. Model. Mechanobiol.* **19**, 221-232 (2020).

39. F. Boselli, J. Vermot, *Methods* **94**, 129-134 (2016).

40. D. Beis *et al.*, *Development* **132**, 4193-4204 (2005).

41. G. Luxan, G. D'Amato, D. MacGrogan, J. L. de la Pompa, *Circ. Res.* **118**, e1-e18 (2016).

42. L. A. Timmerman *et al.*, *Genes Dev.* **18**, 99-115 (2004).

43. J. L. de la Pompa *et al.*, *Nature* **392**, 182-186 (1998).

44. E. Steed *et al.*, *Nat. Commun.* **7**, 11646 (2016).

45. L. M. Goddard *et al.*, *Dev. Cell* **43**, 274-289 (2017).

46. B. Lai *et al.*, *Am. J. Physiol Heart Circ. Physiol* **315**, H1293-H1303 (2018).

47. A. D. Egorova *et al.*, *Circ. Res.* **108**, 1093-1101 (2011).

48. T. Banjo *et al.*, *Nat. Commun.* **4**, 1978 (2013).

49. R. Ferreira, H. Fukui, R. Chow, A. Vilfan, J. Vermot, *J. Cell Sci.* **132**, (2019).

50. A. L. Duchemin, H. Vignes, J. Vermot, R. Chow, *Curr. Opin. Genet. Dev.* **57**, 106-116 (2019).

51. A. L. Duchemin, H. Vignes, J. Vermot, *Elife.* **8**, (2019).

52. J. Schottenfeld, J. Sullivan-Brown, R. D. Burdine, *Development* **134**, 1605-1615 (2007).

53. K. Sekimizu *et al.*, *Development* **131**, 2521-2532 (2004).

54. P. Campinho, P. Lamperti, F. Boselli, A. Vilfan, J. Vermot, *Cell Rep.* **31**, 107505 (2020).

55. K. Yamamoto, R. Korenaga, A. Kamiya, J. Ando, *Circ. Res.* **87**, 385-391 (2000).

56. K. Yamamoto, H. Imamura, J. Ando, *Am. J. Physiol Heart Circ. Physiol* **315**, H1477-H1485 (2018).

57. J. P. Green *et al.*, *Cardiovasc. Res.* **114**, 324-335 (2018).

58. R. A. North, *Physiol Rev.* **82**, 1013-1067 (2002).

59. A. L. Armesilla *et al.*, *Mol. Cell Biol.* **19**, 2032-2043 (1999).

60. C. P. Heisenberg, Y. Bellaiche, *Cell* **153**, 948-962 (2013).

61. T. Mammoto, D. E. Ingber, *Development* **137**, 1407-1420 (2010).

62. T. Merle, E. Farge, *Curr. Opin. Cell Biol.* **55**, 111-118 (2018).

63. S. Donat *et al.*, *Elife.* **7**, (2018).

64. F. Gunawan *et al.*, *J. Cell Biol.* **218**, 1039-1054 (2019).

65. J. Pestel *et al.*, *Development* **143**, 2217-2227 (2016).

66. J. Li *et al.*, *Nature* **515**, 279-282 (2014).

67. K. Nonomura *et al.*, *Proc. Natl. Acad. Sci. U. S. A* **115**, 12817-12822 (2018).

68. C. B. Kimmel, W. W. Ballard, S. R. Kimmel, B. Ullmann, T. F. Schilling, *Dev. Dyn.* **203**, 253-310 (1995).

69. L. Herwig *et al.*, *Curr. Biol.* **21**, 1942-1948 (2011).

70. A. Muto, M. Ohkura, G. Abe, J. Nakai, K. Kawakami, *Curr. Biol.* **23**, 307-311 (2013).

71. Y. Wang *et al.*, *Development* **137**, 3119-3128 (2010).

72. Y. Wakayama, S. Fukuhara, K. Ando, M. Matsuda, N. Mochizuki, *Dev. Cell* **32**, 109-122 (2015).

73. B. S. Clark *et al.*, *Development* **139**, 1599-1610 (2012).

74. S. Fukuhara *et al.*, *Dev. Biol.* **393**, 10-23 (2014).

75. H. Fukui *et al.*, *Dev. Cell* **31**, 128-136 (2014).

76. K. Asakawa *et al.*, *Proc. Natl. Acad. Sci. U. S. A* **105**, 1255-1260 (2008).

77. J. Aramburu *et al.*, *Science* **285**, 2129-2133 (1999).

78. A. K. Patra *et al.*, *Nat. Immunol.* **14**, 127-135 (2013).

79. J. R. Hove *et al.*, *Nature* **421**, 172-177 (2003).

80. J. Salle *et al.*, *J. Cell Biol.* **218**, 771-782 (2019).

81. H. Tanimoto, J. Salle, L. Dodin, N. Minc, *Nat. Phys.* **14**, 848-854 (2018).

82. S. Korzh *et al.*, *BMC. Dev. Biol.* **8**, 84 (2008).

83. Z. Sun *et al.*, *Development* **131**, 4085-4093 (2004).

84. Z. Liu *et al.*, *Nat. Commun.* **10**, 1839 (2019).

85. E. Berdougo, H. Coleman, D. H. Lee, D. Y. Stainier, D. Yelon, *Development* **130**, 6121-6129 (2003).

86. Y. P. Hung *et al.*, *Elife.* **6**, (2017).

87. H. Fukui *et al.*, *Elife.* **7**, (2018).